



**HAL**  
open science

## Voluminous Silica Precipitated from Martian Waters during Late-stage Aqueous Alteration

Lu Pan, John Carter, Cathy Quantin-Nataf, Maxime Pineau, Boris Chauviré, Nicolas Mangold, Laetitia Le Deit, Benjamin Rondeau, Vincent Chevrier

► **To cite this version:**

Lu Pan, John Carter, Cathy Quantin-Nataf, Maxime Pineau, Boris Chauviré, et al.. Voluminous Silica Precipitated from Martian Waters during Late-stage Aqueous Alteration. *The Planetary Science Journal*, 2021, 2 (2), pp.65. 10.3847/PSJ/abe541 . hal-03407619

**HAL Id: hal-03407619**

**<https://hal.science/hal-03407619v1>**

Submitted on 10 Dec 2021

**HAL** is a multi-disciplinary open access archive for the deposit and dissemination of scientific research documents, whether they are published or not. The documents may come from teaching and research institutions in France or abroad, or from public or private research centers.

L'archive ouverte pluridisciplinaire **HAL**, est destinée au dépôt et à la diffusion de documents scientifiques de niveau recherche, publiés ou non, émanant des établissements d'enseignement et de recherche français ou étrangers, des laboratoires publics ou privés.



Distributed under a Creative Commons Attribution 4.0 International License



# Voluminous Silica Precipitated from Martian Waters during Late-stage Aqueous Alteration

Lu Pan<sup>1,2</sup> , John Carter<sup>3</sup> , Cathy Quantin-Nataf<sup>1</sup> , Maxime Pineau<sup>4</sup> , Boris Chauviré<sup>5</sup> , Nicolas Mangold<sup>4</sup> ,  
Laetitia Le Deit<sup>4</sup> , Benjamin Rondeau<sup>4</sup> , and Vincent Chevrier<sup>6</sup> 

<sup>1</sup> Univ. Lyon, Lyon 1, ENS Lyon, CNRS, LGL-TPE, F-69622, Villeurbanne, France; [lu.pan@sund.ku.dk](mailto:lu.pan@sund.ku.dk)

<sup>2</sup> University of Copenhagen, GLOBE institute, Centre for Star and Planet Formation, Copenhagen, Denmark

<sup>3</sup> Institut d'Astrophysique Spatiale, CNRS, Université Paris-Sud, Orsay, France

<sup>4</sup> Université de Nantes, Laboratoire de Planétologie et Géodynamique (LPG), UMR-CNRS 6112, Nantes, France

<sup>5</sup> Université Grenoble-Alpes, CNRS, Grenoble, France

<sup>6</sup> University of Arkansas, Arkansas Center for Space and Planetary Sciences, USA

Received 2020 June 14; revised 2020 December 20; accepted 2021 February 3; published 2021 April 1

## Abstract

Mars' transition from an early “warm and wet” to a “cold and dry” environment left fingerprints on the geological record of fluvial activity on Mars. The morphological and mineralogical observations of aqueous activity provided varying constraints on the condition and duration of liquid water on the Martian surface. In this study, we surveyed the mineralogy of Martian alluvial fans and deltas and investigated the hydrated silica-bearing deposits associated with some of these landforms. Using CRISM data, we identified 35 locations across Mars with hydrated silica in proximity to fans/deltas, where the spectral characteristics are consistent with immature or dehydrated opal-A. In a few stepped fans/deltas, we find hydrated silica occurs within the bulk fan deposits and form sedimentary layers correlated with elevation. Meanwhile, in the older fans/deltas, silica mostly occurs at distal locations, and the relation to primary sedimentary deposits is more complex. We propose that the hydrated silica-bearing deposits in stepped fans/deltas likely formed authigenically from Martian surface waters, mainly during the Late Hesperian and Early Amazonian. These silica-bearing deposits could be a tracer for the temperature or duration of water involved in the formation of these deposits, given more precise and detailed observations of the sedimentary context, accessory minerals, the concentration of hydrated silica, and sediment-to-water ratio. Therefore, we consider that silica-bearing deposits should be among the most critical samples to investigate for future Mars missions, which are accessible in the landing sites of Mars 2020 and ExoMars 2022 missions.

*Unified Astronomy Thesaurus concepts:* [Mars \(1007\)](#); [Planetary surfaces \(2113\)](#); [Surface composition \(2115\)](#); [Hydrosphere \(770\)](#); [Planetary structure \(1256\)](#)

*Supporting material:* figure set

## 1. Introduction

Liquid water flowed on the surface of Mars before 3.5 billion years ago, building a broad diversity of aqueous and potentially habitable environments. The valley networks, deltas, alluvial fans, and paleolakes observed from orbit (e.g., Mangold 2004; Kite et al. 2017) and in situ by landed missions (e.g., Grotzinger et al. 2015) suggest the presence of long-lasting continued runoff and large volumes of liquid water on the surface of Mars that were most prevalent during the Noachian and Hesperian periods, but in some cases extended to Late Hesperian and Amazonian (e.g., dendritic networks in Valles Marineris; Mangold 2004). Conversely, the mineralogical record of past aqueous activity preserved immature minerals (e.g., smectites, opaline silica), whose survival until today point to limited water–rock interaction and diagenesis after their formation (Tosca & Knoll 2009). To reconcile these different observations and better understand the climate of Mars through time, we need to reexamine the duration, timing, and physical states of past aqueous environments on Mars. Here, our investigation focuses on the mineralogy of the sedimentary deposits of surface water activity on Mars, specifically the

hydrated silica associated with the fans and deltas, to understand the evolutionary pathway of the Martian climate through time.

Hydrated silica ( $\text{SiO}_2 \cdot n\text{H}_2\text{O}$ ) is a common weathering product of basaltic rocks, the main constituent of Mars' surface (Shoji & Masui 1971; Ping et al. 1988; Opfergelt et al. 2011; McLennan 2003). Hydrated silica has been identified on Mars from orbit (e.g., Bandfield 2008; Bishop et al. 2008; Milliken et al. 2008; Skok et al. 2010; Goudge et al. 2012; Carter et al. 2013a; Hauber et al. 2013; Smith et al. 2013; Pan & Ehlmann 2014; Sun & Milliken 2018; Pineau et al. 2020) and in situ with landed missions (e.g., Squyres et al. 2008; Rice et al. 2010; Rapin et al. 2018). More recently, silica-bearing deposits have been found in the Mars 2020 landing site Jezero Crater (Tarnas et al. 2019; Horgan et al. 2020), as well as Oxia Planum, the selected landing site for the European Space Agency's ExoMars rover (Carter et al. 2016; Quantin-Nataf et al. 2021). The precipitation of silica occurs when a solution becomes oversaturated with respect to the mineral phase (quartz, amorphous silica) as it reaches certain physical and chemical conditions (e.g., Alexander et al. 1954; Siever 1962; Sjöberg 1996). Thus, silica-bearing deposits can be an essential indicator of the temperature and, to a lesser extent, pH of the aqueous environment in which they are formed. Silica-bearing deposits, especially when they have undergone any degree of diagenesis, could also indicate the time/duration of exposure to



Original content from this work may be used under the terms of the [Creative Commons Attribution 4.0 licence](#). Any further distribution of this work must maintain attribution to the author(s) and the title of the work, journal citation and DOI.

water Tosca & Knoll (2009). In addition, various forms of hydrated silica (and their diagenetic transformation products) have been characterized as having high astrobiological potential, due to their ability to entrap and preserve microfossils and other chemical and morphological biosignatures (Knoll et al. 1985; Trewin 1996; Lazzeri et al. 2017; McMahon et al. 2018; Abu-Mahfouz et al. 2020; Teece et al. 2020). Locating and investigating the silica-bearing deposits in fluvial settings will thus bring new understanding to the climate conditions in which fluvial morphology and silica co-occurred and highlight important scientific targets for ongoing and future in situ observations.

On Mars, terminal fluvial deposits have been identified to be widespread on the interior of impact craters that are connected to incised channels (e.g., Cabrol & Grin 1999; Irwin et al. 2004; Moore & Howard 2005; Di Achille & Hynek 2010). Many of these deposits are interpreted as alluvial fans, formed by sediment deposition into a conical shape due to the lateral expansion of flow (e.g., Moore & Howard 2005; Kraal et al. 2008a), while others show inverted channel avulsion on the surface that is interpreted as branched deltas (e.g., Fassett & Head 2005; Pondrelli et al. 2005). On Mars, additionally, a type of “stair-step” or “terraced” fan-shaped sediment, which lacks typical terrestrial analog, has been proposed to form due to one of these scenarios: a deltaic deposition with increasing water base level (e.g., de Villiers et al. 2013), erosional wave actions (e.g., Ori et al. 2000), or multipisode debris-flow-dominated alluvial processes (Di Achille et al. 2006b). Here we study silica-bearing deposits associated with alluvial fans and deltas on Mars using a combination of available orbital image data sets. Based on the geological context of the hydrated silica-bearing deposits, we discuss their possible formation scenarios and their implications for the Martian environment. Our analysis aims at providing an overview to guide the investigation of silica-bearing deposits in alluvial fans and deltas during future in situ explorations and Mars Sample Return missions, which could bring crucial constraints on the conditions (volume, temperature, pH, and duration/extent) of past Martian waters.

## 2. Method

### 2.1. A Global Survey of Silica-bearing Fans and Deltas

The Compact Reconnaissance Imaging Spectrometer for Mars (CRISM) is a hyperspectral imaging spectrometer that acquires data of the Martian surface in the near-infrared wavelength range (1–4  $\mu\text{m}$ ), which enables the identification of hydrated minerals, including hydrated silica (Murchie et al. 2007, 2009). We built our global data sets based on a selection of CRISM images from two sources: (i) locations from a previous global survey of CRISM images (Carter et al. 2013a) filtered by morphology indicators as alluvial fans and deltas; and (ii) a database of alluvial fans and deltas identified in previous morphology analysis (e.g., Cabrol & Grin 1999, 2001; Ori et al. 2000; Moore et al. 2003; Irwin et al. 2005; Kraal et al. 2008a; Di Achille & Hynek 2010), where we confirmed CRISM coverage in proximity to these deposits. The complete list of the fans and deltas investigated in this study with required CRISM coverage is given in Table A1, with relevant references where available (see Appendix A).

We analyzed the select CRISM images following the previous data processing methodology, in which we calculated

the ratioed images based on a column-averaged denominator of selected pixels below the  $1.5\sigma$  threshold within the spectral parameter range (Carter et al. 2013b; Pan et al. 2017). Hydrated silica was identified based on absorption bands at 1.4, 1.9  $\mu\text{m}$  and a broad, characteristic 2.2  $\mu\text{m}$  band due to vibrational modes of hydroxyl groups in molecular water ( $\text{H}_2\text{O}$ ) and silanol groups ( $\text{Si-OH}$ ; Anderson & Wickersheim 1964; Langer & Florke 1974). The averaged spectra were obtained from a region of interest within contiguous pixels exhibiting a similar NIR reflectance value and texture in CRISM images (Figure B1). The spectra with possible identification of hydrated silica were classified based on the confidence level in spectral feature identification, quantified by the 1.9 and 2.2  $\mu\text{m}$  band depths (see Appendix B, Figure B2). The classification only applied to the select spectra chosen for each location, while spectral features may vary within a given fan/delta location.

### 2.2. High-resolution Images and Digital Elevation Model (DEM)

We utilized imagery data sets of various spatial resolutions to investigate the silica-bearing deposits. We used the CTX mosaic provided by the Murray Planetary Visualization Lab as a base map (Dickson et al. 2018). The High Resolution Imaging Experiment (HiRISE;  $\sim 25$  cm/pix; McEwen et al. 2007) and Context Camera (CTX,  $\sim 6$  m/pix; Malin et al. 2007) images of locations of interest were downloaded and calibrated using the Integrated Software for Imagers and Spectrometers (ISIS) routine enabled by the MarsSI platform (Quantin-Nataf et al. 2018). All of the visible images and CRISM spectral data with various resolutions were coregistered to the CTX mosaic using the georeferencing application of the Quantum GIS (QGIS) software and manually selecting the control points. The outlines of the fans were digitized by tracing the base of the fans also within a QGIS project. For the key sites with stereo image coverage, we processed the stereo images to generate DEMs with the USGS Ames pipeline (Beyer et al. 2018). Topographic profiles, elevation, slope, and maximum fan volumes were measured for locations with a clear morphologic context. We estimated the volume of the fan deposit with a flat-bottom assumption, which likely overestimates the total volume of the deposit.

### 2.3. Spectral Analysis of Hydrated Silica

The free and hydrogen-bonded water species ( $\text{H}_2\text{O}$  and  $\text{Si-OH}$ ) within hydrated silica vary in different types of silica due to their varying crystallinity and formation pathways (e.g., Anderson & Wickersheim 1964; Langer & Florke 1974; Boboň et al. 2011; Rice et al. 2013; Chauviré et al. 2017). To understand the type of silica deposited with fans and deltas, we calculated spectral parameters as demonstrated in previous studies (Rice et al. 2013; Sun & Milliken 2018; Pineau et al. 2020). It has been shown that the most distinguishing spectral parameters are the location of the minimum of the 1.4  $\mu\text{m}$  band and the shape of the 1.9 and 2.2  $\mu\text{m}$  bands. The minimum of the 1.4  $\mu\text{m}$  band is calculated upon the linear-continuum-removed spectra anchored at 1.35 and 1.44  $\mu\text{m}$ . We calculated the relative band depths using several different approaches. Following Rice et al. (2013), the 1.91 and 1.96  $\mu\text{m}$  band depths are calculated using the classic band-depth formula

(Equation (1)):

$$\text{BD} = 1 - \frac{R_b}{R_c}, \quad (1)$$

where  $R_b$  is the reflectance of the band position and  $R_c$  is the reflectance calculated for the continuum made up of both shoulders of the absorption band. The band ratio of 2.21 to 2.26  $\mu\text{m}$  was calculated by fitting a double Gaussian centered at  $\sim 2.21$  and  $\sim 2.26$   $\mu\text{m}$  on the continuum-removed spectra, equivalent to the method of Sun & Milliken (2018). Finally, we applied the new spectral parameters (CRC1.4 and CRC1.9) based on terrestrial opals, which allows hydrothermal and low-temperature weathering hydrated silica to be discerned and has been shown to be potentially applicable to Mars (Chauviré et al. 2017; Pineau et al. 2020). The spectra were first smoothed using the Savitzky-Golay algorithm with third-degree polynomial functions and a moving average window of about 7 to 9 spectels (Savitzky & Golay 1964; Steinier et al. 1972). For the two absorption bands at 1.4 and 1.9  $\mu\text{m}$ , two anchor points were chosen at  $\sim 1.30$  and  $\sim 1.60$   $\mu\text{m}$ , and  $\sim 1.85$  and  $\sim 2.10$   $\mu\text{m}$  respectively. Then, we calculated the two band-depth ratios: BDR, the real band-depth ratio of the inflection points at 1.46 and 1.96  $\mu\text{m}$  (Equation (2)), and  $\text{BDR}_*$ , the virtual band-depth ratio of the same wavelength using the linear continuum between the minimum of the 1.4/1.9  $\mu\text{m}$  band and the anchor point at  $\sim 1.60$   $\mu\text{m}$ ,  $\sim 2.10$   $\mu\text{m}$ , respectively. Eventually, the concavity-ratio criterion (CRC) parameters were calculated as

$$\text{CRC} = \frac{\text{BDR}}{\text{BDR}_*}. \quad (2)$$

The errors in the CRC calculations were calculated empirically by shifting the two anchor points over  $\pm 3$  spectels. As a result, several CRC were calculated for each absorption band of each spectrum (over 35 combinations). The CRC-retained value is the average of all the calculated values, and the errors represent the standard deviation ( $1\sigma$ ). The more convex the absorption band is, the higher the CRC value is. The CRC1.9 parameter is highly sensitive to the atmospheric residual at 1.96–2.1  $\mu\text{m}$  due to  $\text{CO}_2$  absorption, and the CRC1.4 parameter can be affected when absorption is small in comparison with the noise. Therefore, we removed spectra with particularly weak 1.4 and 1.9  $\mu\text{m}$  bands from this analysis, and plotted with error bars calculated using shifted anchor points to provide a first-order evaluation of the effect of noise. A full data set of the calculated CRC parameters can be found in Figure B3.

### 3. Results: Mineralogy, Distribution, and Context for Silica-bearing Deposits

Within the 98 locations of previously identified alluvial fans or deltas with CRISM coverage, we identify 62 with confirmed or possible identification of hydrated minerals (see Appendix A). Among them, 35 locations (Figure 1) with associated fluvial deposits are found with hydrated silica-bearing deposits, including the two selected landing sites at the Jezero Crater and Oxia Planum, for the Mars 2020 and ExoMars 2022 missions, respectively. Because the identification of hydrated minerals using CRISM images can be confounded by dust cover, partial coverage of the fan/delta,

and exposures beneath the spatial resolution of the images ( $\sim 18$ – $36$  m/pixel), the number of identified locations gives a lower limit to the global distribution of hydrated silica occurrences in fans and deltas. Regardless, hydrated silica, which is rather spatially limited compared to other hydrous minerals on Mars (e.g., Fe/Mg phyllosilicates; e.g., Carter et al. 2013a; Ehlmann & Edwards 2014; Sun & Milliken 2015), is found to occur relatively frequently in alluvial fans and deltas. We have studied the spectral and imagery data set covering all 35 locations, and here below we summarize the main findings in these silica-bearing fans and deltas in terms of their spatial extent, spectral characteristics, and correlation to morphology (Table 1). All of these silica-bearing deposits identified are observed within the spatial extent of sedimentary basins that have been affected by fluvial activity. Most of the fluvial deposits form distinct morphology of alluvial fans or deltas, while others have preserved evidence for a paleolake (e.g., Melas Chasma; Metz et al. 2009; Weitz et al. 2015) and at proximity to fluvial landforms like channels (e.g., Maja Valles). Silica-bearing deposits found within the Maja Valles channel are also at the terminus of smaller, better-preserved fluvial channels, but no clear fan/delta morphology is identified (Figure C1).

We identify hydrated mineral detections using CRISM spectra with absorption bands around 1.4  $\mu\text{m}$ , 1.9  $\mu\text{m}$ , and a broad 2.2  $\mu\text{m}$  due to vibrational modes of hydroxyl groups in molecular water ( $\text{H}_2\text{O}$ ) and silanol groupings Si–OH (Figure 2(A)). Although there are variabilities in the band position and band shapes of 1.4, 1.9, and 2.2  $\mu\text{m}$  absorptions, the particular width and shape of the 2.2  $\mu\text{m}$  absorption features in the spectra distinguish hydrated silica from Al-phyllosilicates or sulfates (Figures 2(B), (C)). The spectra have been classified into four categories (C1–C4) based on their band depths at 1.9 and 2.2  $\mu\text{m}$  to indicate different levels of spectral signature (see Appendix B). The C1–C2 spectral classes have prominent spectral features at 1.4, 1.9, and 2.2  $\mu\text{m}$  that match the band shape and width of the hydrated silica in the spectral library and lab experiments. The C3–C4 spectra often show the broad 2.2  $\mu\text{m}$  band but with a much weaker signal close to the level of noise, which does not allow a thorough examination of the shape of the absorption bands. The presence of hydrated silica is a plausible explanation of these spectra with a 2.2  $\mu\text{m}$  band, but we cannot exclude the possibility that other hydrated minerals with a 2.2  $\mu\text{m}$  band, including Al-phyllosilicates, gypsum, or jarosite, could be present in minor amounts in a mixture (Figure 2(C)). Spectral features, including band positions and depths, can be used to identify different types of hydrated silica (e.g., opal-A, opal-CT), with implications for their origin. The Martian infrared spectra of hydrated minerals often show a weaker 1.4  $\mu\text{m}$  band compared to their terrestrial counterparts, resulting in a small signal-to-noise ratio at this wavelength, which limits our ability to interpret the spectral band center. However, for the C1–C2 spectral detection of silica-bearing deposits, the 1.4  $\mu\text{m}$  absorption due to the Si–OH overtone occurs at  $\sim 1.38$   $\mu\text{m}$ , atypical of terrestrial laboratory spectra of opaline silica in ambient conditions of which the overtones commonly occur at 1.41  $\mu\text{m}$  (Figure 2(B)). In comparison with laboratory measurements of terrestrial silica of various structure and origin, the CRISM spectra with a minimum band position at 1.38–1.4  $\mu\text{m}$ , and the shape of the 2.2  $\mu\text{m}$  feature is consistent with immature silica (e.g., hydrated glass or opal-A) under Martian atmospheric conditions (Figures 2(D) and (E)). The



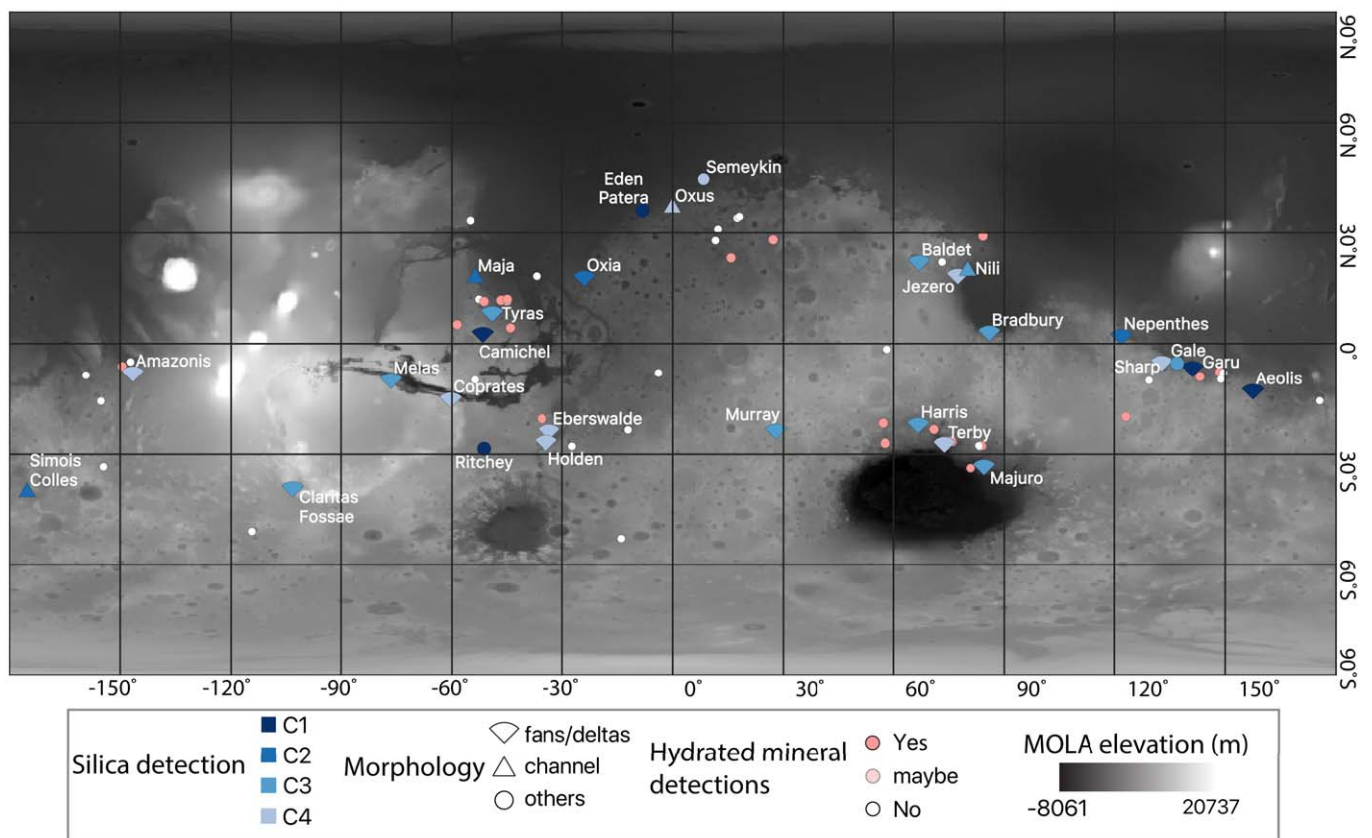


**Figure 1.** Global distribution of fluvial deposits associated with hydrated silica-bearing deposits. This map highlights the locations with fluvial morphology found with hydrated minerals in a previous global survey (Carter et al. 2013a). Locations found with hydrated silica detections are highlighted in blue and those without a clear silica detection in pink. The silica spectral signatures of different confidence are categorized into C1–C4 based on their band depths at 1.9 and 2.2  $\mu\text{m}$  (see Section 2.1). For locations found with silica-bearing deposits, fan symbols are used to represent silica-bearing deposits associated with fans or deltas; triangles represent silica found associated with deposits within a fluvial channel; dots represent other types of geological settings (e.g., a volcanic caldera, periglacial setting). The background is MOLA in equirectangular projection.

minimum positions of the 1.4  $\mu\text{m}$  band used to identify different types of silica are controlled by the mineral structure and do not overlap with wavelength regions that are affected by artifacts and atmospheric residuals. The band shapes of the 1.9 and 2.2  $\mu\text{m}$  features, however, may be altered if there is significant atmospheric residual at 2  $\mu\text{m}$  due to  $\text{CO}_2$  compared to the absorption features. Therefore, we highlight C1, C2 spectra with well-defined absorption bands so that the influence by noise or atmosphere is minimal (Figure 2). In the meantime, the 1.4 and 1.9  $\mu\text{m}$  band shapes constrained by the CRC parameters are consistent with the spectral features of silica in terrestrial sediments formed during low-temperature weathering processes (Figure 2(F), Figure C1). Having tested a large data set (Figure C1), we highlight those with a more robust signal (Figure 2(F)), because the CRC parameters reflect subtle concavity change, which is prone to noise or atmospheric residual. Other hydrated minerals may also alter the band shape, resulting in small variations in the CRC parameters, but their impact should be minor because their presence cannot be resolved using present orbital data.

The silica-bearing deposits inside fans/deltas are associated with layered deposits, and their spectral signatures are correlated with elevations, as in the case of Aeolis (Figure 3(A)), Camichel (Figure 3(B)), and Garu (Figure 3(C)). The elevation profiles suggest the correlation of these siliceous layers with the sedimentary layers within the fans, but no visible outcrop of

planar bedding is found at these locations. Other deposits of silica occur in spatially discontinuous patches in distal sediments and are correlated with lower elevation or greater distance to the source, as in the case for Eberswalde (Figures 3–4), Jezero (Figures 3–5), and Oxia Planum (Figures 3–6). Aeolis, for example, is a stepped fan/delta with robust silica detection corresponding to the entire fan deposits. There are three topographic steps in the fan, which show varying Si–OH band depth with a continuously increasing 2.21  $\mu\text{m}$  absorption band depth with decreasing elevation (Figures 4(A), (B)). In the Camichel and Garu fans, the silica-bearing deposits are found in discrete, continuous horizontal layers of 50 m in thickness (Figures 3–2, 3, 5), correlated with a fine-grained, smooth texture in HiRISE images (Figure 6). Cross sections on the walls of small impact craters expose subsurface materials, which show silica spectral signature is present along the rim down to  $\sim 10$  m depth (Figure 4(C)). In the Camichel and Garu fans, the silica deposits are found only in discrete, continuous horizontal layers of  $\sim 50$  m in thickness (Figures 4 (B), (C), and 5), correlated with fine-grained, smooth texture in HiRISE images (Figure 6). At Claritas Fossae and Amazonis, silica-bearing deposits are also found over layers of sedimentary deposits, but with weaker and less continuous spectral signatures. At these locations, silica could be exposed locally from dust cover or less well preserved, inhibiting our ability to assess the distribution of silica-bearing deposits in these images fully. At the other fans/deltas, hydrated

**Table 1**  
Locations with Hydrated Silica Identified in Proximity to Fluvial Morphology<sup>a</sup>

Latitude (°N)	Longitude (°E)	Name	Basin <sup>b</sup>	CRISM ID (e.g.,)	Spectra (Category)	Morphology	Location <sup>c</sup>	Reference (fan/delta)	Reference (silica)	Age <sup>d</sup> Ga (ref.)
-12.7	157.5	Aeolis	C	FRT000086B7	C1	Stepped	Bulk		1, 2	<3.5 <sup>e</sup>
2.7	-51.7	Camichel	C	HRL0000927F	C1	Stepped	Bulk	3-6	4,6	0.57 (4)
-6.6	141.2	Garu	C	HRL0000C549	C1	Stepped	Bulk	4,7	1	3.46-0.4 (4)
-39.2	-103.1	Claritas Fossae	C	FRT0000944A	C3	Stepped	Bulk	8	1	>H (8)
-8.0	-146.6	Amazonis	C	FRT0001BB1F	C4	Stepped	Bulk	9-10, 6	1	0.6-0.8 <sup>f</sup> (9)
-5.1	132.9	Sharp	C	FRT000064CE	C4	Fan	Distal	11	1	
22.2	66.9	Baldet	C	FRT00008D46	C3	Fan	Distal	12		
-23.8	-33.6	Eberswalde	C	FRT00009C06	C4	Delta	Distal	13-14	1	3.65-3.46 (49)
18.5	77.4	Jezero	C	HRL000040FF	C4	Delta	Distal	15-17	1, 18	>3.5 (50)
17.8	-53.7	Maja	P	HRL0000B48B	C2	Channel	Channel		1	3.5 <sup>g</sup> (19)
-15	-60.3	Coprates	O	FRT00007203	C4	Stepped	Distal	20-22	23	<3.16 (22)
3.2	85.9	Bradbury	P	FRT0000B0CB	C3	Fan	Bulk	24-25	26-28	>3.83 (28)
17.9	-24.0	Oxia	P	ATU0003D04C	C2	Delta	Distal	29-30	29-30	>3 (26)
-9.8	-76.5	Melas	O	FRT00009B66	C3	Erosional <sup>h</sup>	Distal	31-33	33-34	>3 (32)
8.4	-49.1	Tyras	C	HRL0000AB77	C3	Delta	Distal	35	1	3.35-3.63 (4)
-26.7	-34.5	Holden	C	FRT0000474A	C4	Fan	Distal	36-38		3.65-3.46 (49)
-22.0	66.7	Harris	C	HRL00013C12	C3	Fan	Distal	38-39		1N (39)
2.1	121.9	Nepenthes	P	FRT0001D7F0	C2	Delta	Distal <sup>i</sup>	40-41,4	1	1.80 (4)
-40.3	-175.2	Simois Colles	P	FRT00016E5C	C2	Channel	Channel		1	
35.9	-8.2	Eden Patera	O	FRT0000CE47	C1	Other	Other		1	
36.7	-0.1	Oxus	O	FRT0000A3D8	C4	Channel	Channel		1	
44.7	8.4	Semeykin	P	FRT00009E68	C4	Other	Other		1	
-33.2	84.5	Majuro	C	FRT0001642D	C3	Fan	Bulk,Distal	12	46	3.59 (42)
-5.4	137.0	Gale	C	FRT000045F2	C3	Fan, delta	Other	9,43-44	45-46	<3.6 (43-44)
-28.5	-51.3	Ritchey	C	FRT0000AC1F	C1	Other	Other	47-48	48	3.5 (47)
-27.17	73.82	Terby	C	FRT00009A8D	C4	Delta/Other <sup>j</sup>	Distal	51-52	52	eN-H (52)
19.7	80.08	Nili	P	FRT00016655	C3	Channel	Other			
-23.62	27.98	Murray	C	FRS0003D1A2	C3	Fan	Distal			

#### Notes.

<sup>a</sup> Locations where multiple fans and deltas are found (e.g., Harris, Melas) have been grouped together in this table.

<sup>b</sup> Abbreviation for basin type: Crater (C), Plains (P), and Others (O).

<sup>c</sup> Silica location is categorized as "Fan," "Distal," "Channel" or "Other." "Bulk" indicates silica detection on the bulk deposit of the fan/delta, while "Distal" indicates silica detected outside of the bulk fan deposit, in the distal regions of the fan/delta. "Channel" suggests silica is detected within the fluvial channel. "Other" indicates silica detection in close vicinity of a fluvial fan or delta, but they are not directly related to the fluvial morphology, including occurrences on the central peak or central mound of a crater, layered deposits, or the bedrock close to fluvial features.

<sup>d</sup> Age of the fan or delta deposits from previous literature. Abbreviations: H-Hesperian; IN-Late Noachian; eN-Early Noachian.

<sup>e</sup> Age of the floor unit. The crater count over the fan deposits is saturated.

<sup>f</sup> Age of the lake basin based on crater density of the basin floor.

<sup>g</sup> Age of the Maja terminus and Chryse crater floor while younger resurfacing events have occurred (e.g., Chapman et al. 2003).

<sup>h</sup> Erosional remnant of a fan-shaped deposit, where only the top surface is exposed.

<sup>i</sup> Nepenthes is a Gilbert-type delta on top of older deltaic deposits. Silica outcrop at distal locations may belong to older deposits where the fluvial morphology is unclear.

<sup>j</sup> The Terby crater hosts a thick sequence of light-toned layered deposits but lacks the fluvial channels leading to the deposits, which have been interpreted as deltaic deposits (Ansan et al. 2011) or volcanic/aeolian deposits (Wilson et al. 2007).

**References.** (1) Carter et al. (2012), (2) Sun & Milliken (2018), (3) Hauber et al. (2009), (4) Hauber et al. (2013), (5) Popa et al. (2010), (6) Goudge et al. (2012), (7) Di Achille & Hynes (2010), (8) Mangold & Ansan (2006), (9) Cabrol & Grin (2001), (10) Hughes (2012), (11) Irwin et al. (2004), (12) Kraal et al. (2008a), (13) Malin & Edgett (2003), (14) Moore et al. (2003), (15) Fassett & Head (2005), (16) Tarnas et al. (2019), (17) Masursky et al. (1977), (18) Baker & Kochev (1979), (19) Chapman et al. (2003), (20) Weitz et al. (2006), (21) Di Achille et al. (2006b), (22) Grindrod et al. (2012), (23) Weitz et al. (2015), (24) Erkeling et al. (2012), (25) Bramble et al. (2019), (26) Bishop et al. (2008), (27) Bishop et al. (2013), (28) Tirsch et al. (2018), (29) Quantin-Nataf et al. (2021), (30) Carter et al. (2016), (31) Weitz et al. (2003), (32) Quantin et al. (2005), (33) Metz et al. (2009), (34) Williams & Weitz (2014), (35) Di Achille et al. (2006a), (36) Grant & Parker (2002), (37) Pondrelli et al. (2005), (38) Moore & Howard (2005), (39) Williams et al. (2011), (40) Irwin et al. (2005), (41) Kleinhans et al. (2010), (42) Mangold et al. (2012a), (43) Thomson et al. (2011), (44) Le Deit et al. (2013), (45) Seelos et al. (2014), (46) Fraeman et al. (2016), (47) Ding et al. (2015), (48) Sun & Milliken (2014), (49) Mangold et al. (2012b), (50) Mangold et al. (2020), (51) Wilson et al. (2007), (52) Ansan et al. (2011).

silica is only found in small regions of interest (10–50 pixels), preferentially in the distal region, outside of the bulk fluvial deposits (Table 1). In the five stepped fans/deltas where silica detections are correlated with elevation, the volume of the silica-bearing sedimentary rocks varies from 0.15 km<sup>3</sup> to 4.8 km<sup>3</sup> (see Appendix F).

The small surface areas and significant denudation through time prevent an accurate dating of the bulk fan deposits (Palucis et al. 2020), but in many cases, an estimate may be obtained based on the largest crater and stratigraphic relations. The ages of the deltas and fans span from Noachian to Amazonian (see Table 1 and references therein). It is rather

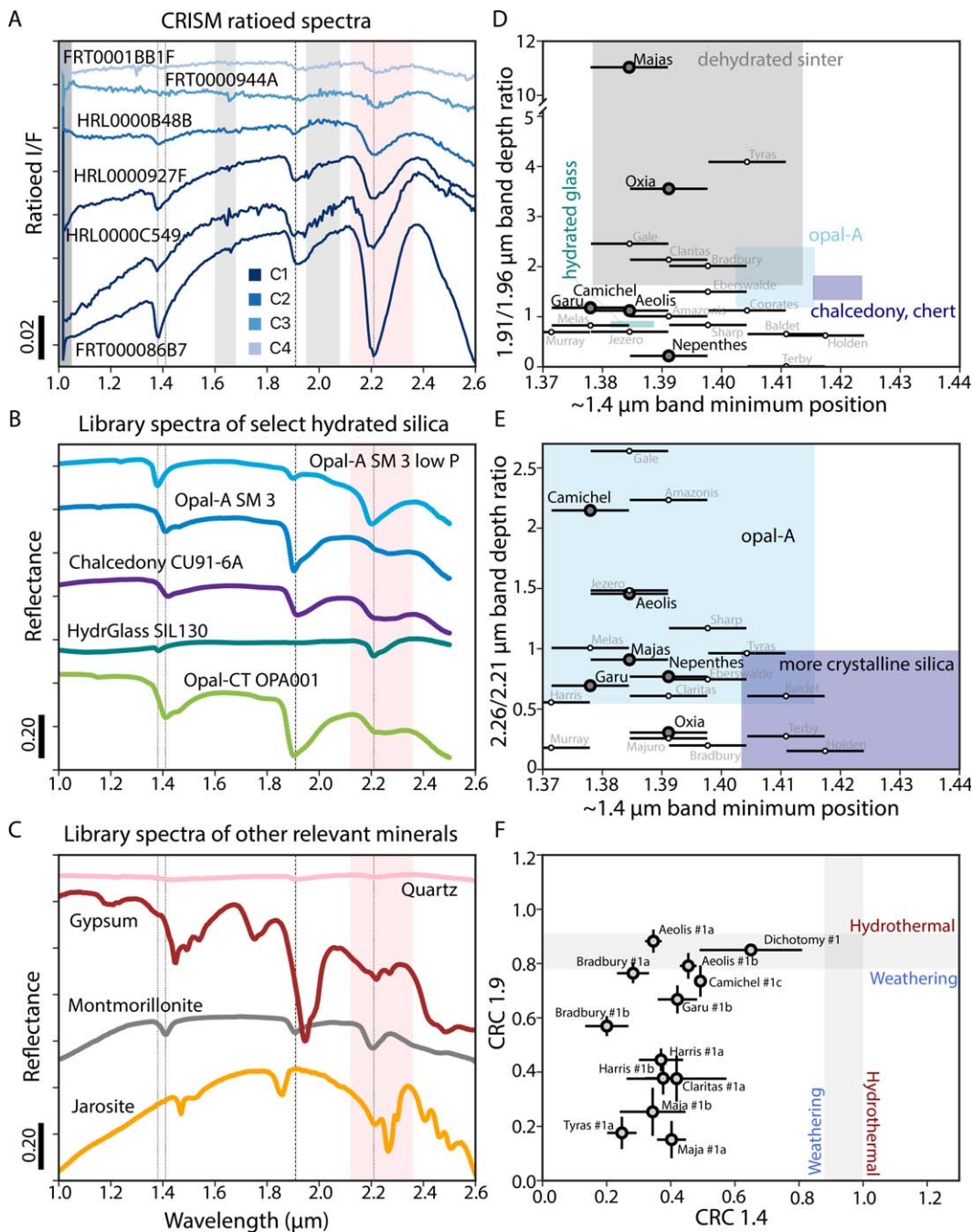


**Figure 2.** Spectral detections of hydrated silica on Mars. (A) Select CRISM spectra of hydrated silica detections with varying certainties in alluvial fans. The gray shaded regions represent wavelengths of CRISM artifacts and atmospheric residuals. The pink shaded region corresponds to the typical  $2.2 \mu\text{m}$  band of hydrated silica. (B) Type laboratory spectra of different varieties of hydrated silica found on Earth. Opal-CT and hydrated glass spectra are from Rice et al. (2013), Opal-A spectra under normal and low-pressure conditions are from Sun & Milliken (2018). The spectrum for chalcedony is from the USGS spectral library (Clark et al. 2007). (C) Relevant mineral spectra for comparison from spectral libraries, including quartz, Al-phyllsilicate, and sulfate (Clark et al. 2007). (D) Plot of the  $1.4 \mu\text{m}$  band minimum position and  $1.91/1.96 \mu\text{m}$  band-depth ratio for select locations (excluding locations with ambiguous context and where the  $1.9 \mu\text{m}$  band is strongly affected by the atmosphere residual). Larger gray dots represent spectra categorized as C1 or C2. The ranges of different types of silica are from Rice et al. (2013). (E) Plot of spectral absorption of the  $1.4 \mu\text{m}$  band position and  $2.21/2.26 \mu\text{m}$  band shape following Sun & Milliken (2018). Larger gray dots represent spectra categorizes as C1 or C2. Blue shaded regions represent the parameter space of opal-A and opal-C/CT, respectively. (F) The plot of the CRC1.9 and CRC1.4 spectral parameters compared to the range of different types of terrestrial silica samples following Pineau et al. (2020). A larger set of spectra (1–4) for each location has been examined. CRC parameters that are affected by atmosphere residual or low signal-to-noise level are not included. The data for panels (D)–(F) are provided as data behind the figure.

intriguing that the strongest spectral signature and spatially extensive (e.g., with continuous outcrop up to 1 km) silica-bearing deposits are found in stepped fans/deltas that formed mostly in the last 3.5 Ga (Table 5). Six stepped fans/deltas in our survey are found with hydrated silica, including Aeolis,

Camichel, Garu, Amazonis, Claritas Fossae, and Coprates. These locations are found with a bulk silica-bearing deposit inside the fan/delta deposits, except for Coprates, where the silica is identified in the distal region outside the bulk deposits. Other than Coprates, all these sedimentary features likely



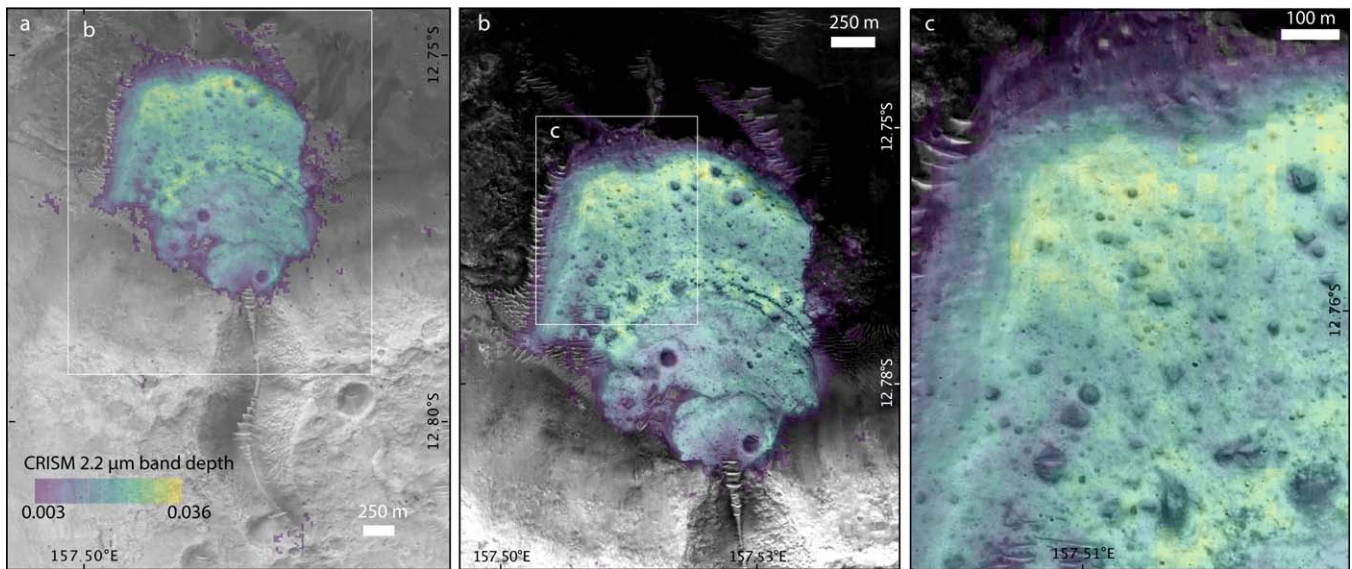


**Figure 3.** Images of the fans and deltas that are found with hydrated silica, with the CRISM spectral parameter overlay showing the locations of the silica detections. (a) The overall context of the fan/delta including inlet channel(s); (b) the fan/delta deposit with silica detection; (c) a zoomed image showing the silica detection. The complete figure set (6 images) is available.

(The complete figure set (6 images) is available.)

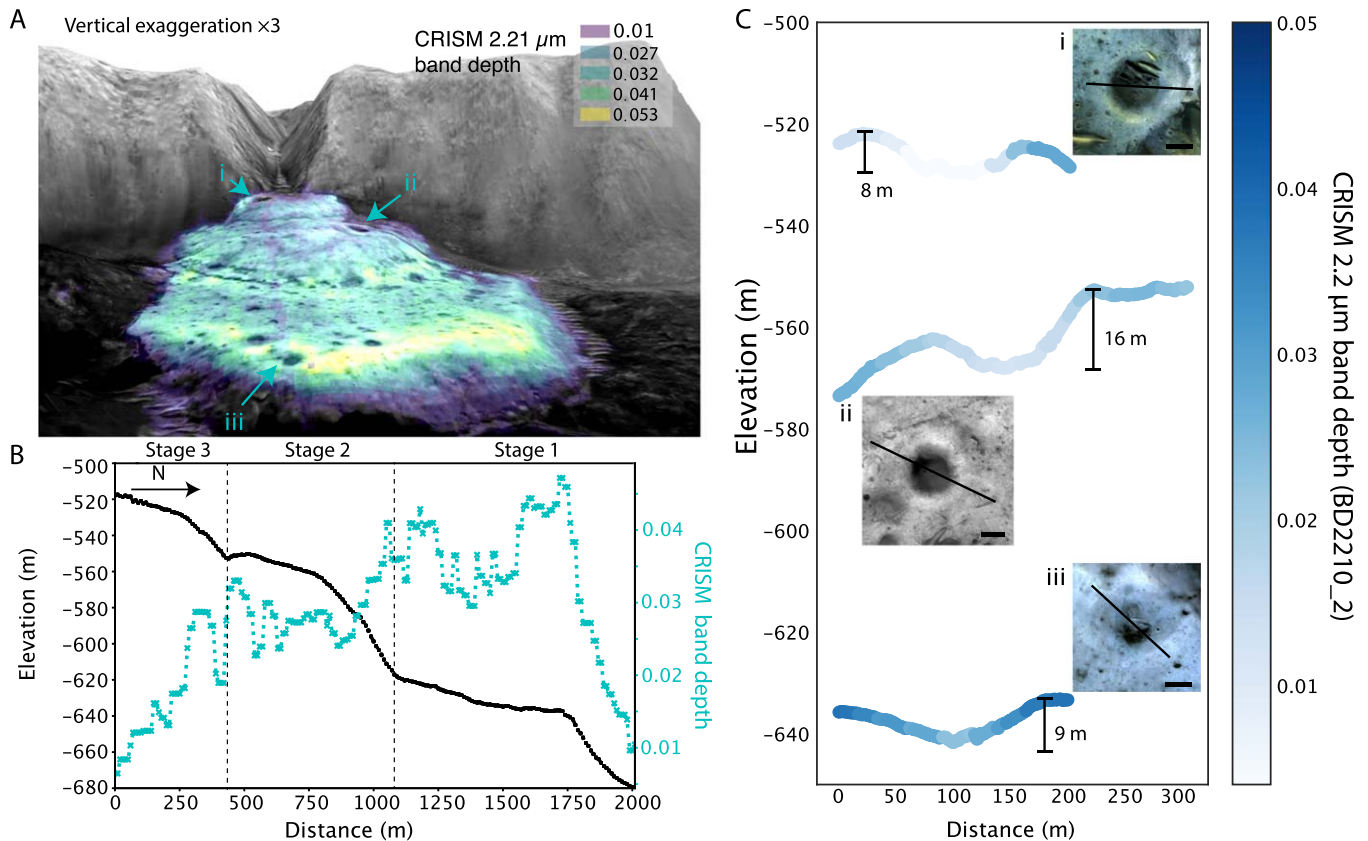


**Figure 4.** Elevation profile of silica detections in the Aeolis fan. Strong silica detections (up to 5%) are identified in the fan deposit. A. 3D exaggeration of the Aeolis fan, overlaid by the CRISM spectral parameter (BD2210\_2) indicating the band depth of 2.2  $\mu\text{m}$  absorption (interpreted as Si-OH). Notations i, ii, iii refer to the craters whose cross-sectional profiles are plotted in (C). (B) The central elevation profile of the same fan from the apex to the toe of the crater in black and the corresponding CRISM parameter in cyan. (C) Cross sections of impact craters where walls are exposed. The floor of the craters is all filled with sand, so the variations of band depths on the crater walls are more reliable indicators of the bedrock. The silica absorption band depth decreases with depth, but the amount of decrease is relatively small, in comparison with the changing strengths of absorption with elevation.



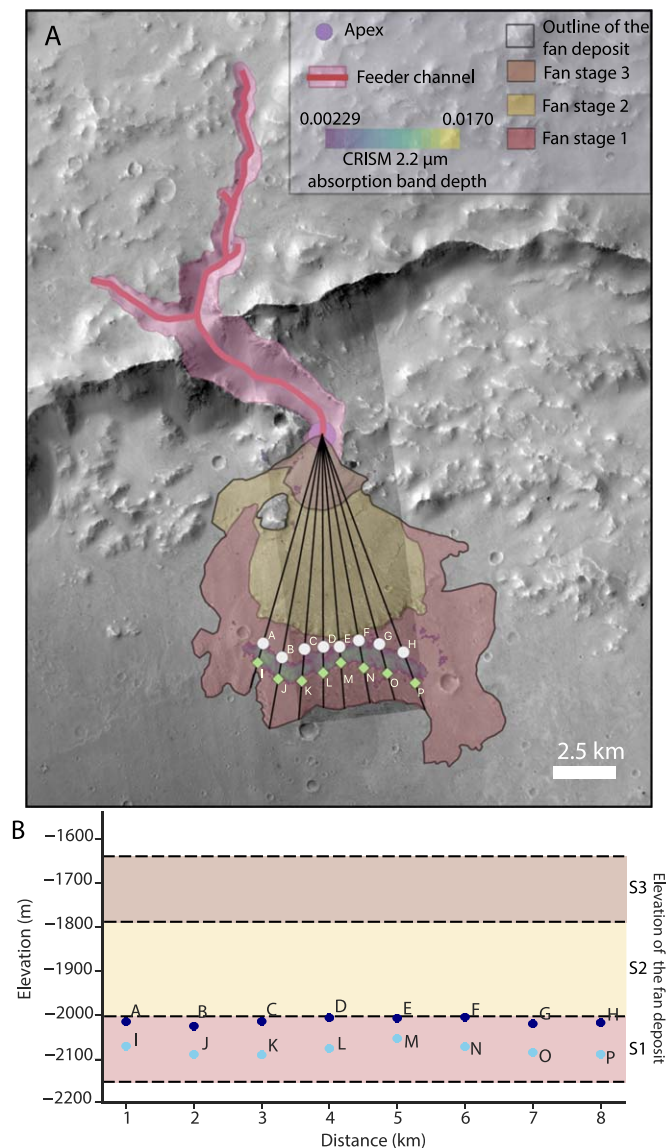


**Figure 5.** Elevation of the silica-bearing deposits of the Camichel fan. (A) Geological map showing the location of different fan stages and the feeder channel connected to the fan. The base map is the HiRISE image PSP\_006941\_1825 and the CTX mosaic. (B) The elevation plot of silica detection with eight different profiles from the apex of the fan to the base of the fan. (A)–(H) are intersections with the upper level of the silica deposit, and (I)–(P) are the lower intersections. Compared to the elevation of the fan, the silica-bearing deposits occur at constant elevation levels.

formed in the last 3.5 Ga: e.g., Camichel (0.57 Ga), Garu (0.4–3.46 Ga), Amazonis (0.68 Ga). The tectonic features in the regional context of Claritas Fossae are dated to be Hesperian, suggesting the fluvial activity was active at or after the Hesperian (Mangold & Ansan 2006). The Aeolis fan is deposited on a crater floor unit where the nine largest craters give a crater count age of 3.5 Ga with continuous resurfacing at least until 0.5 Ga (Figure D1).

On the contrary, most of the older deltas (e.g., Eberswalde, Jezero) and fans (e.g., Murray, Holden) have silica-bearing deposits in very localized outcrops and discontinuous patches in the distal region of the delta (e.g., with a continuous outcrop of up to 100 m), and the silica spectral features are relatively weaker. Given the lack of complete outcrop of these silica-bearing deposits, we cannot exclude the possibility that the

apparent differences in spatial extent and spectral signature may be related to the preservation states, rather than a primary feature of the outcrop. If fan/delta formation involved multiple stages of fluvial activities, the crater-count-based age of the fans and deltas at these locations only give an upper limit to the age of silica formation.

In addition, there are other locations including Bradbury, Majuro, and possibly Maja where silica are identified in the bulk sedimentary deposit, but do not have the typical stepped morphology. The distinct geologic context and aqueous activity at each location will have to be investigated in detail in future studies to elucidate their relationships to mineralogy. While these fans'/deltas' formations are scattered in time, given their observed well-preserved features and stratigraphic relations, they likely indicate the last active fluvial activity in the fluvial system they are connected to (e.g., Mangold et al. 2020).

#### 4. The Origin of Hydrated Silica in Fans and Deltas

Hydrated minerals, mostly Fe/Mg phyllosilicates, have been previously identified within fans and deltas, where the proposed origins for these hydrated minerals have been put forward as either detrital (e.g., Ehlmann et al. 2008; Murchie et al. 2009; Milliken & Bish 2010; Poulet et al. 2014) or authigenic (e.g., Dehouck et al. 2010; Ansan et al. 2011; Bristow & Milliken 2011; Mangold et al. 2012a; Hauber et al. 2013; Poulet et al. 2014). Unlike Fe/Mg phyllosilicates, hydrated silica-bearing deposits may also occur in the form of volcanic glass, hydrothermal deposits (including sinters), as in the case for silica detections in volcanic calderas in Nili Patera (Skok et al. 2010). The spectral signature, the spatial distribution, and the volumetric measurements in comparison with sedimentary deposits are key to unraveling the geologic process in which silica-bearing deposits were formed in Martian alluvial fans and deltas.

##### 4.1. The Spectral Features of Hydrated Silica

The shorter band center of the 1.4 μm absorption feature in association with the broad 2.2 μm band matches spectral features with deposits enriched in amorphous or dehydrated silica. Possible explanations of the spectral signature include the formation of hydrated glass (Rice et al. 2013; Smith et al. 2013), as well as a dehydrated opal-A under Martian atmospheric conditions (Poitras et al. 2018; Sun & Milliken 2018) or elevated temperature (Boboň et al. 2011). Here the geologic context (co-occurrence with fluvial deposits and smooth, high albedo features) supports the origin as a silica deposit from water–rock interaction rather than detrital glass. The susceptibility to weathering of volcanic glass also means they are less likely to persist in a prolonged fluvial setting. Additionally, the shape of the 1.4 and 1.9 μm bands characterized by the CRC parameter shows that these CRISM spectra are more consistent with terrestrial silica (opal-A/CT) from low-temperature weathering (Pineau et al. 2020), for select locations where the 1.4 and 1.9 μm bands are well defined and not affected by atmospheric residual. The spectral signature including the shorter wavelength position of the 1.4 μm band, the lack of concavity of the 1.9 and 2.2 μm bands agree with that of relatively pristine and dehydrated opal-A, as compared to the silica spectra that are often found in aeolian/transported deposits on Mars, consistent with opal-CT (Sun & Milliken 2018; Pineau et al. 2020). The spectral characteristics

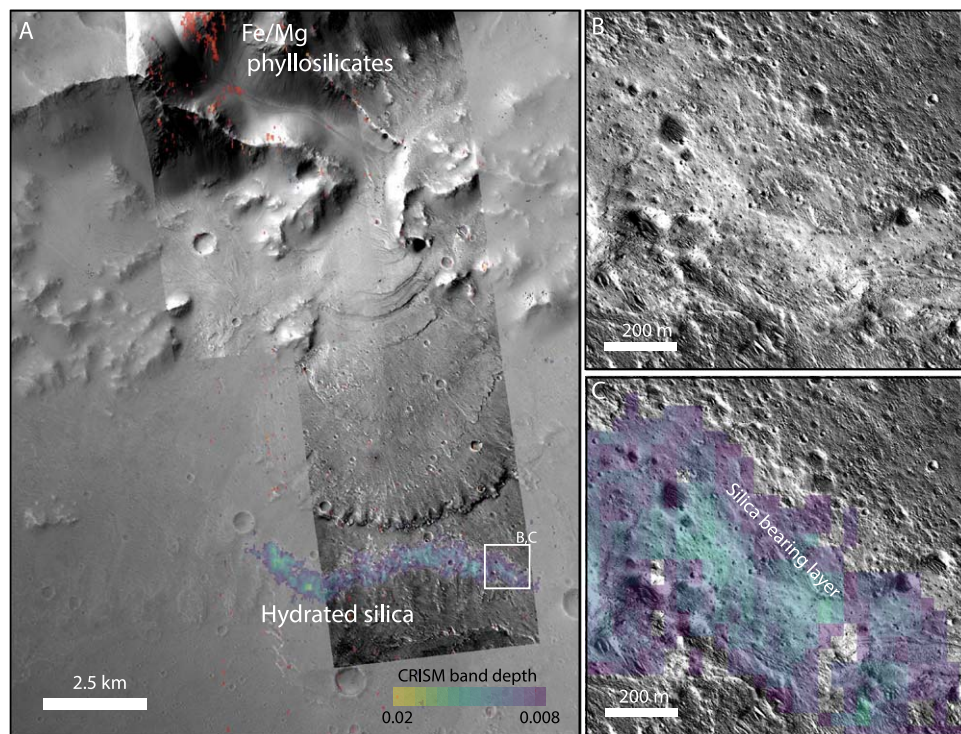


**Figure 6.** HiRISE images (ESP\_027287\_1830 and PSP\_006941\_1825) registered on the CTX mosaic over the Camichel fan. (A) The Fe/Mg phyllosilicate detections on the channel walls and silica deposit near the base of the fan. The white box shows the location of (B) and (C). (B) Close-up of the HiRISE image ESP\_027287\_1830 showing the texture of the silica-bearing deposit. (C) The same extent as (B) with an overlay of the CRISM spectral parameters of  $2.2 \mu\text{m}$  band depth showing the location of the silica detection. Note the distinctly smooth, fine-grained texture and higher albedo relative to the upper and lower beds. The strongest silica detection (light blue) is associated with the smooth, light-toned layer on the HiRISE image.

support the interpretation of dehydrated opal-A formed in low-temperature weathering processes ( $<50^\circ\text{C}$ ), congruous with the geologic context of altered fluvial deposits.

Such an immature spectral feature indicates the hydrated silica associated with these fans and deltas may be primary deposits, in contrast to the mobilized silica in present-day eolian sediments as shown by Sun & Milliken (2018). Opal-A-bearing deposits on Earth transform to opal-C within a few million years at a temperature of  $50^\circ\text{C}$  (Compton 1991). Albeit the rate constant of such transition at low temperature is rather uncertain, a complete opal-CT to quartz conversion should occur within 100–400 Ma on Martian conditions given reasonable assumptions (Tosca & Knoll 2009). The presence of such an immature type of silica indicated by the spectral features associated with fans or deltas thus implies very limited duration of water availability, if at all, after their initial deposition.

#### 4.2. Distribution and Context of Silica in Association with Fluvial Morphology

The  $2.2 \mu\text{m}$  band depth indicative of hydrated silica is found to be correlated with the elevation of the deposit in the Aeolis fan (Figures 8(A) and 4) and formed as a continuous layer in Camichel and Garu (Figures 3(B), (C)), in concordance with the layering when observed. The variations in band depth could be due to changes in lighting geometry, exposures of fresh surfaces from dust, as well as hydrated silica concentration and grain size. Lighting geometry influences the reflectance level observed, but it is found that the spectral band depth, calculated from the ratio of reflectance, should vary only by a few percent when the phase angle is smaller than  $60^\circ$  (Shepard & Cloutis 2011; Ruesch et al. 2015). At Aeolis, the phase angle between

$39.5^\circ$  and  $45.5^\circ$  could not have caused significant variations in spectral band depth. If the band-depth variations are caused by dust cover, we expect to have dust accumulation and therefore reduced band depths at lower elevation and locations with gentler slope, contrary to our observations. Therefore, the spectral band-depth variation at Aeolis is likely correlated to the physical or chemical changes in the sediments, possibly due to variations in silica concentration or grain size (e.g., Clark et al. 1990). Either silica concentration increases with lower elevation, or silica is found in smaller grain-sized particles at lower parts of the fan. The distribution of silica preferentially in the distal regions is in contrast to the expected behavior at a hydrothermal source. As temperature decreases exponentially with time and distance to the source, silica precipitation should be expected to decrease over time and with greater distance if hydrothermal fluid were flowing on the surface, without additional heating sources (see Appendix E). The thickness of the silica-bearing deposits can be indicative of their formation mechanisms. At Aeolis, the silica band depth decreases with depth within the craters but remains above the detection limit down to  $\sim 10$  m in elevation (Figure 4). Formation as a continuous layer with correlating texture and constant elevation suggests silica precipitation occurred within the 50 m thick deposits in Camichel and Garu (Figures 3, 5, 6). In addition, thin coatings and rinds 100s of microns thick would easily be removed within a million years even with the limited erosion rates ( $0.01\text{--}0.1 \text{ nm yr}^{-1}$ ) of Amazonian Mars (Golombek & Bridges 2000). These observations indicate that the silica detection is not limited to the upper micron-thick layer on top of these deposits, in contrast to the micron-sized silica coatings of Hawaiian basalt, which forms rather quickly

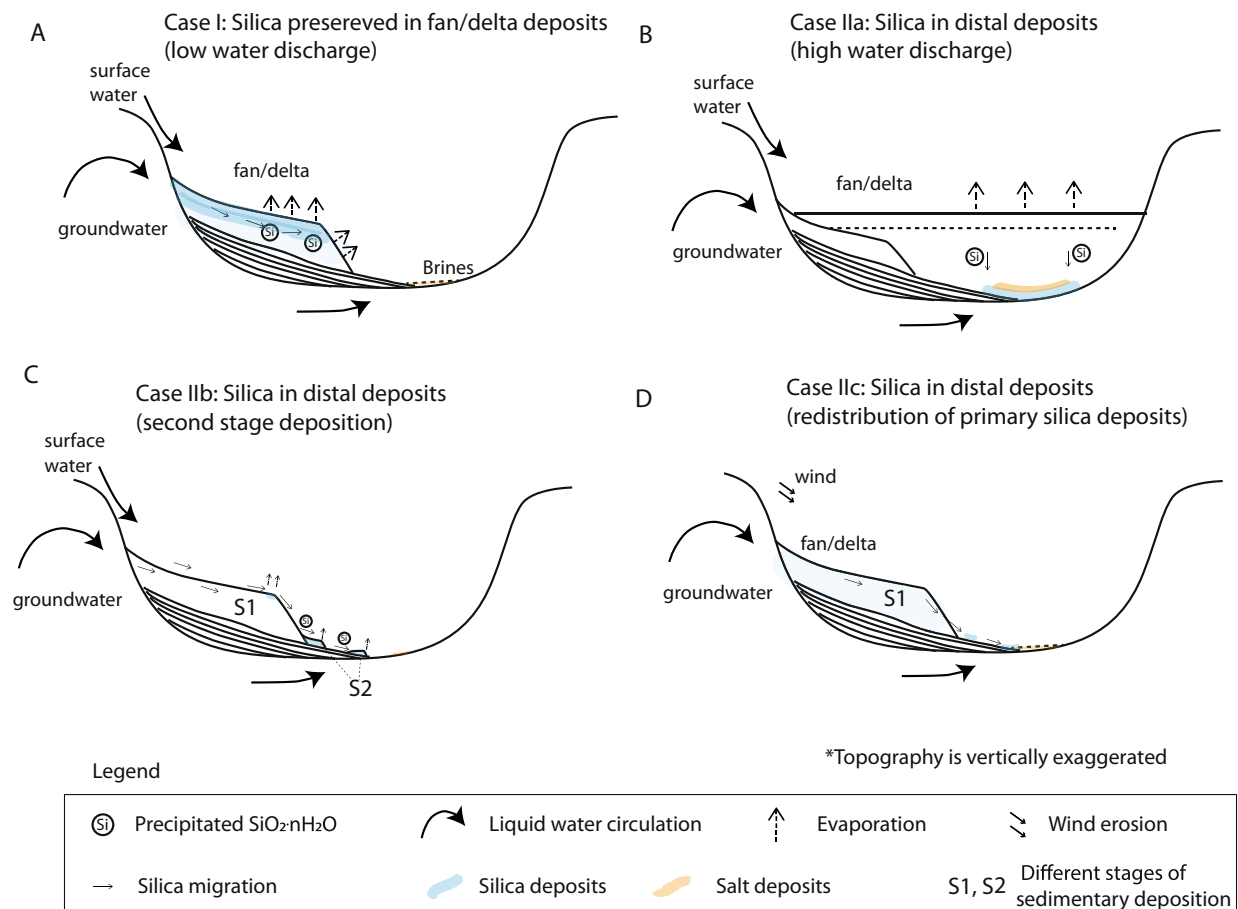


**Figure 7.** Schematic model of silica precipitation within fan/delta with different amounts of water discharge. The topographic profiles are vertically exaggerated to show the flow within the fan/delta deposit.

as shown in previous studies (Minitti et al. 2007; Chemtob et al. 2010).

The source regions of these fans and deltas lack silica-bearing outcrops. The lack of observation may be due to dust cover, as tens of microns of dust cover could inhibit our ability to detect hydrous minerals using CRISM data. However, unlike Fe/Mg phyllosilicates, which are widespread in the southern highlands of Mars, silica-bearing deposits have only been found in small, localized deposits (e.g., Bishop et al. 2008; Skok et al. 2010), most of which with smaller spatial extent than the deposits in fans and deltas. We have not yet identified any location in which widely distributed silica-bearing deposits occur in the source region of the fan or delta deposit, although some isolated regions have been found with hydrated silica outside the sedimentary basin (e.g., Melas and Coprates e.g., Milliken & Bish 2010; Carter et al. 2012; Le Deit et al. 2012). Unless there exist widespread silica-bearing deposits in the subsurface that have not been detected so far, the silica observed here, in particular in the stepped fans/deltas where bulk silica-bearing materials are found, likely are not detrital materials.

#### 4.3. The Origin of Silica-bearing Deposits

As discussed in the previous sections, there are no identified widespread silica deposits indicating the hydrated silica-bearing deposits could have been transported from elsewhere as detrital sediments. If the silica deposits were buried in the subsurface within the source rocks, they might have acted as a

lubricator resulting in the basal slide similar to the effect of clay minerals (Watkins et al. 2015), thus forming fan-shaped deposits in front of a wall scarp. The fans and deltas investigated in this study are connected to well-defined inlet channels (e.g., Figure 3), in contrast to the typical landforms of landslides with an arcuate breakaway zone in the source region. Thus, the morphology and lack of source region for these silica-bearing deposits are inconsistent with the landslide scenario formed with subsurface silica deposits.

Alternatively, silica, which is easily mobile during water-rock interaction, could dissolve in pore waters and reprecipitate (e.g., Williams & Crerar 1985; Sjöberg 1996; McLennan 2003). While terrestrial alluvial fans in semiarid locations can be carbonate cemented (Blissenbach 1964; Nickel 1985), different pH and water chemistry may have been involved in silica formation in alluvial fans/deltas on Mars. The silica-bearing layers occurring at a near-constant elevation relative to the current geoid at each location indicate formation directly from surface standing bodies of water or the intersection of the groundwater with the surface. In either scenario, the precipitation of silica co-occurred with the deposition of the sediments in the alluvial fans or deltas. The late diagenetic event could have also precipitated silica deposits, as multiple-stage diagenesis has been observed in the Meridiani Planum (e.g., Christensen et al. 2004; McLennan et al. 2005; Frydenvang et al. 2017; Rapin et al. 2018). To be consistent with the observed distribution of silica-bearing deposits, a preexisting layer of sediments with higher porosity or permeability should



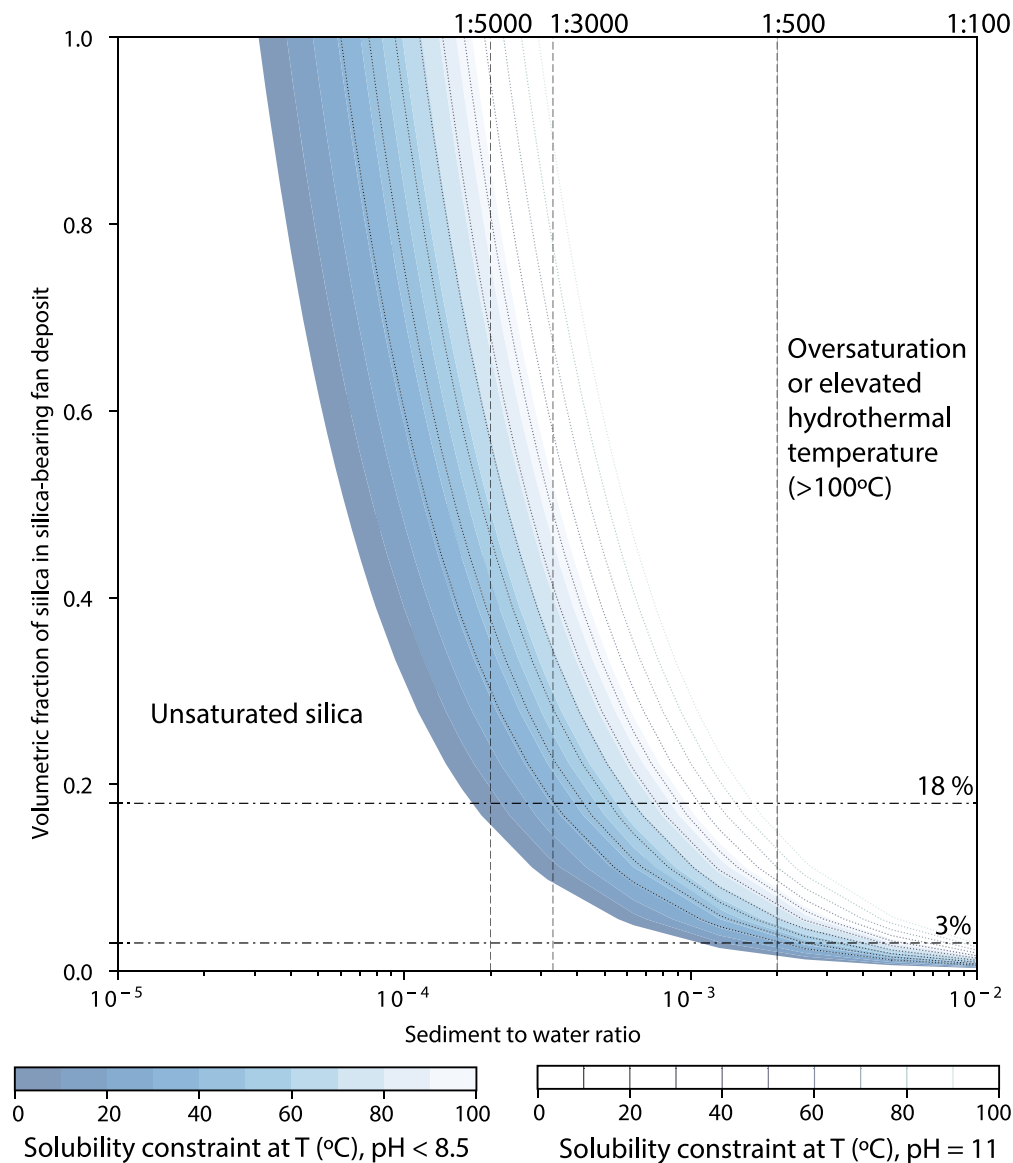


**Figure 8.** Estimated solubility of silica with varying volumetric fraction of silica and sediment to water ratio. The contours give the theoretical solubility constraints at temperatures from 0 °C to 100 °C and acidic-neutral pH (>8.5) and pH = 11 (Dove 1995; Sjöberg 1996; Gunnarsson & Arnórsson 2000). We show a wide range of sediment-to-water ratios from typical terrestrial rivers (1:5000, 1:3000) to mass concentration flows (1:500, 1:100). The range of silica solubility constraint is calculated from the equilibrium constant of amorphous silica.

be present that allows later diagenetic events to occur in a constricted sedimentary layer. If such late diagenetic events did occur, we would expect silica in locations other than the fan or delta deposits (e.g., in the floor of the basin), which has not been identified so far. It is also unlikely a late diagenetic event would significantly change the macroscale texture of the sedimentary layer, as shown to be distinct from sediments above and below (Figure 6). While we do not favor a late-diagenesis scenario for the bulk silica deposits in stepped fans/deltas, it is likely such events may have occurred in many locations investigated here where silica is present as a discontinuous outcrop in the distal region. For example, aqueous activity involves multiple lake levels in the Gale crater (Palucis et al. 2016), and the hydrated silica could have formed during the latest stage of diagenesis, as shown with the high-silica fracture-associated halos in the Murray formation (e.g., Frydenvang et al. 2017).

Considering the lack of source region, the spectral signature and the correlation with topography, the formation of silica-bearing deposits likely have occurred at the same time or shortly after the deposition of the sediments. In particular, we propose silica precipitation in the stepped fans/deltas (e.g., Aeolis, Camichel, Garu) was active in conditions with a relatively low water discharge in the most recent epoch on Mars (Figure 7(A)). In such an environment, water reaches silica oversaturation due to evaporation or change in chemical or physical conditions and begins to precipitate silica, enveloping sedimentary grains within sedimentary deposits as siliceous cement. Silica could be then accumulated as they are adsorbed to sedimentary particles and transported down the section within the fan/delta deposits. The formation of silica thus follows either the surface water upon the fan deposits or groundwater seepage at a specific level, making continuous deposits within the fan/delta.

Apart from the occurrence in the bulk sedimentary deposits in stepped fans/deltas, silica preferentially occurs at distal locations in areally restricted, discontinuous outcrops in most older fans and deltas. The preferred distal occurrence suggests a different condition during sedimentation or higher degrees of subsequent modifications compared to the bulk silica-bearing deposits. During the primary fluvial process, if the water discharge is relatively high to the sediment flux and silica concentration is beneath saturation, silica precipitation within the sedimentary deposits can be hindered. In this scenario, silica would be dissolved in standing bodies of water and only begin to precipitate in a mixture with other salts or clay minerals on the basin floor as water evaporates (Figure 7(B)). Alternatively, the reactivation of a fluvial system over time (Hauber et al. 2013; Mangold et al. 2020) may have induced multiple sedimentary stages, and volumetrically smaller deposits may have occurred after the bulk of the fan or delta has been formed, leaving localized silica deposits (Figure 7(C)). Otherwise, if hydrated silica were initially deposited in the bulk sedimentary deposits, they may be subject to secondary processes that redistributed silica due to a longer duration of groundwater activity, aeolian reworking, and redeposition, thus making it more challenging to preserve silica-bearing deposits within the fan or delta (Figure 7(D)). In all proposed scenarios, the silica-bearing deposits recorded the water volume and conditions during its primary precipitation, but in the older deltas or fans (Figures 7 (B)–(D)), the current outcrops may be partially related or unrelated to the primary silica deposits. Detailed context analysis in situ may help distinguish these scenarios, which cannot be determined from orbit.

#### 4.4. Mass Balance with Water Volume Estimates

In a scenario where hydrated silica has precipitated during the fluvial activity forming the fans and deltas in place, one could make reasonable estimates of the water volume and condition based on mass balance. The volume of water involved should match between the mineralization of silica-bearing deposits ( $V_{\text{H}_2\text{O}_{-\text{Si}}}$ ) and the formation of the geomorphologic features ( $V_{\text{H}_2\text{O}_{-\text{sed}}}$ ).

$$V_{\text{H}_2\text{O}_{-\text{sed}}} \sim V_{\text{H}_2\text{O}_{-\text{Si}}} \quad (3)$$

The first approach consists of estimating water volume through the volume of the sediment, regardless of composition. Because it is impossible to obtain a grain size distribution from orbital images, we rely on the sediment-to-water ratio ( $R_{\text{sed}/\text{water}}$ ) to understand the order of magnitude of the volume of water involved (Equation (4)):

$$V_{\text{H}_2\text{O}_{-\text{sed}}} = \frac{V_{\text{sed}}}{R_{\text{sed}/\text{water}}} \quad (4)$$

Terrestrial rivers have an average sediment-to-water ratio of 1:5000 (Dietrich et al. 2003), while in arid or semiarid regions (e.g., Chile), the ratio is close to 1:3000 (Pepin et al. 2010; Palucis et al. 2014). However, it has been shown in previous laboratory experiments that the typical stepped morphology observed in many Martian alluvial fans (Figure 3–6) could be formed during a concentration flow with a high sediment-to-water ratio (i.e., ca. 1:10–1:100; Kraal et al. 2008b; Kleinhans et al. 2010). As we consider the integrated volume of water

throughout active fluvial processes, the sediment-to-water ratio for one specific mass flow would underestimate the integrated water volume, especially if standing bodies of water were present for a sufficiently long time. It is also unclear if the sedimentation did occur with a very high mass concentration (ca. 1:10). Therefore, here we adopt the 1:100 ratio as a reasonable upper bound. The uncertainties regarding the sedimentation processes indicate significant variations in the order of magnitude of the water volume involved in the formation of these fluvial deposits. For a maximum volume of 0.15 km<sup>3</sup> of sediments that have been deposited in Aeolis, this would indicate  $\sim 15$  km<sup>3</sup> (1:100) to  $\sim 750$  km<sup>3</sup> (1:5000) liquid water involved in this sedimentary process.

On the other hand, the amount of silica precipitates also helps constrain the amount of water involved, where we need to consider the solubility of amorphous silica under different temperatures and pH ( $K_{\text{Si}}(T, \text{pH})$ ) and the concentration of silica in the sediments ( $f_{\text{Si}}$ ; Equation (5)):

$$V_{\text{H}_2\text{O}_{-\text{Si}}} = \frac{V_{\text{Si}} \times f_{\text{Si}}}{K_{\text{Si}}(T, \text{pH})} \quad (5)$$

Silica remains as monomeric silicic acid in solution at acidic to neutral pH, where the solubility for different silica species is correlated with temperature (Gunnarsson & Arnórsson 2000; Equation (6)):

$$\text{Am. Silica: } \log(K) = -8.476 - 485.24/T - 2.268 * 10^{-6}T^2 + 3.068 \log(T) \quad (6)$$

Near pH = 9, the first dissociation of silicic acid ( $\text{H}_4\text{SiO}_4$ ) became dominant until pH = 12 (Dove 1995; Sjöberg 1996), following the equilibrium constant (Equation (7)):

$$\text{pH} + \log\left(\frac{[\text{H}_3\text{SiO}_4^-]}{[\text{H}_4\text{SiO}_4]}\right) = pK_{1,1} = 9.8 \quad (7)$$

Complications of cation species in solution forming complexes, adsorption, surface area, and particle size could control the precipitation rate of silica-bearing deposits kinetically (e.g., Williams et al. 1985; Williams & Crerar 1985; Dove 1995). Here we performed our calculations considering thermodynamic equilibrium during the silica precipitation process (Equations (6) and (7); see Appendix E) without the complication of the dissolution rate and kinetics of silica precipitation.

We take Aeolis as an example because all three fan steps show evidence of hydrated silica. Given the average thickness of the silica deposit up to  $\sim 10$  m in each step of the fan, it is estimated that at least 20% of the bulk fan comprises silica, but their concentration cannot be uniquely constrained from orbit. We consider a reasonable range of total silica concentration within the bulk of the fan between 3% (assuming 15% silica in the upper 10 m) and 18% (assuming the upper 10 m consist of up to 90% silica based on observations of terrestrial siliceous sediments (Ledevin 2013; Trower & Lowe 2016), as well as rover analysis and remote sensing (Squyres et al. 2008; Bandfield et al. 2013; Figure 8). Provided the constraints given by volumetric measurements and solubility calculations (Equations (4)–(7)), we find that a silica fraction close to 18% is consistent with a terrestrial-river-like sediment-to-water ratio, while a silica fraction close to 3% may indicate a much

higher sediment-to-water ratio and therefore a debris-flow-like process of sedimentation (Figure 8). The solubility constraints do not preclude precipitation at a lower temperature ( $<50\text{ }^{\circ}\text{C}$ ) in any of the scenarios, consistent with the indications from CRC parameters.

#### 4.5. Implications for Future Explorations

To refine water volume estimates, both the sediment-to-water ratio and the volumetric fraction of silica could be more precisely determined with in situ observations that consist of high-resolution imaging and compositional analysis that provide information on the grain size distribution of the sediments and silica concentration. Accessory minerals that might be present in minor amounts would provide additional constraints on the pH of water during silica formation. Such information, as well as detailed modeling of silica precipitation processes, would be crucial to pinpoint the environment in which these fluvial deposits and hydrated silica formed, providing novel insights into the temperature of Martian waters at the time of formation. Other than its potential to constrain the aqueous environments, hydrated silica also has important astrobiological implications (McMahon et al. 2018). It is worth noting that pervasive siliceous sedimentary deposits exist in the Archean geologic records on Earth (Siever 1962), where textural information at the centimeter to millimeter scale exist and detailed compositional and isotopic analysis has been carried out to constrain the water chemistry and the formation pathways of these sediments (e.g., van den Boorn et al. 2007; Ledevin 2013; Trower & Lowe 2016; Kleine et al. 2018). Comparative studies of silica samples considering the sedimentary cycles on Earth and Mars, as well as their potential to preserve organic matter in silica-bearing deposits, make compelling goals for future analysis on returned samples from Mars.

### 5. Conclusions and Implications for Future Exploration

As presented in this study, we identified a global process where silica precipitation occurs in close proximity with alluvial fans and deltas. Notably, five out of six stepped fans/deltas that formed during late-stage fluvial activity (0.4–3.5 Ga) show evidence of silica formation concurrently with the formation of sedimentary deposits, while other older fans and deltas are identified with hydrated silica mostly in the distal region with a few exceptions. The hydrated silica found at these locations typically has a 1.38–1.4  $\mu\text{m}$  band with broad 1.9 and 2.2  $\mu\text{m}$  absorptions, consistent with amorphous silica (glass) or dehydrated opal-A. CRC parameters indicate spectral proximity to terrestrial silica-bearing deposits formed under low-temperature weathering conditions ( $<50\text{ }^{\circ}\text{C}$  as defined in

Chauviré et al. 2017). In a few typical locations, these silica-bearing deposits are correlated with different sedimentary stages within the fan, follow near-planar layers, and lack an obvious source. We suggest that the hydrated silica-bearing deposits formed in stepped fans/deltas are likely authigenic products through precipitation from Martian waters in close relation with the fluvial activity that resulted in the formation of fans and deltas as terminal fluvial deposits of river channels. The order-of-magnitude volume estimate based on the current understanding of fluvial systems on Mars is consistent with the volume of water needed to precipitate silica deposit, given a sediment-to-water ratio between 1:100 and 1:5000 during the aqueous episode forming the sedimentary deposits. In the case of Aeolis, for example, it is possible to precipitate the required volume of silica in a relatively low-temperature environment, consistent with the spectral parameter calculations. The immature nature of these hydrated silica identified suggests very limited timescale (e.g., a few million years) for these aqueous activities that resulted in opaline silica formation and they are likely the latest aqueous events at each location. Given new measurements of grain size distributions and silica concentration in future in situ observations, it would be possible to constrain the volume, temperature, and chemistry of the water that formed these silica-bearing fan and delta deposits. The study highlights the potential of these silica-bearing deposits to understand past climate conditions on Mars, in addition to their astrobiological potentials to incorporate and preserve organic molecules, demonstrating their necessity to be considered as critical scientific targets for future Mars missions, including rover explorations and Mars Sample Return.

The authors would like to thank the instrument teams for CRISM, HiRISE, and CTX for providing the valuable data sets, and Jay Dickson and the Murray Lab at Caltech for generating and sharing the CTX global mosaic. This project has received funding from the European Union's Horizon 2020 research and innovation program under the Marie Skłodowska Curie grant agreement No. 751164, ANR project ANR-18-ERC1-0005, and Carlsberg Foundation grant CF18\_1105. We thank the two anonymous reviewers for the constructive reviews that improved this manuscript.

### Appendix A Database for Global Survey of Fans and Deltas

In this section, we provide the database including all sites in the literature and in our CRISM data survey (Table A1). We indicate the references for locations identified in previous studies, as well as the silica and other hydrated mineral detection results for locations with required CRISM data coverage.



**Table A1**  
Database for Global Survey

LAT	LON	Name	CRISM	Previously Reported	Other Hydrated Minerals	Silica Detections
-12.76	157.52	Aeolis	FRT000086B7 MSP00003AB6		Y	Y
-8.97	143.18		FRT0000A3B6		Y	N
-6.49	141.24	Garu	HRL0000C549	Di Achille & Hynek (2010)	N	Y
-5.02	132.85	Sharp	FRT00014869 FRT000064CE	Irwin et al. (2004)	Y	Y
			FRT0001963E MSP0000610B			
-10	129.38		FRT000063D8		N	N
-19.93	123.11	Cimmeria	FRT0000537A	Kraal et al. (2008a)	Y	maybe
2.2	122.3	Dichotomy2	FRT0000CB64		Y	Y
2.13	121.87	Dichotomy1	FRT000147E0 FRT00016525	Irwin et al. (2005)	Y	Y
			FRT0001D7F0			
3.5	86.12		FRT00009657 FRT000085D7		Y	N
3.1	85.95	Lybia Montes, Bradbury Crater	FRT0000B0CB		Y	Y
3.43	85.92		FRT0001FDD7		Y	N
2.81	85.88	Bradbury Crater	FRS00027210		Y	N
2.89	85.7	Bradbury Crater	FRT0001E2F2 FRT000240DF		Y	N
			FRT0001ECEC			
3.27	84.96	Hashir	FRT0001647D		Y	maybe
-33.2	84.5	Majuro Crater	FRT0001642D FRT00010D71	Kraal et al. (2008a)	Y	Y
-27.77	83.97	McCauley Crater 1	FRT0001B8E1		Y	N
-27.68	83.68	McCauley Crater 2	FRT00019C7E		Y	N
-27.91	83.24	McCauley Crater 3	FRS000272DC	Moore & Howard (2005)	N	N
-27.68	83.13	McCauley Crater 4	FRT00020C76		N	N
-33.75	80.86		FRT000238D3		maybe	N
19.7	80.08		FRT00016655		Y	Y
18.56	77.35	Jezero Crater	HRL000040FF FRT00005850	Fassett & Head (2005)	Y	Y
			FRT000047A3 FRT00005C5E			
-26.64	75.9	Runanga Crater 1	FRT00021C00		Y	N
-26.6	75.66	Runanga Crater 2	FRS0002AA8F		Y	N
-27.82	74.19	Terby Crater 1	FRT0001C779		maybe	maybe
-27.57	74.23	Terby Crater 2	FRT000059DF		Y	N
-27.17	73.82	Terby Crater 3	FRT00009A8D		Y	Y
-23.37	70.98		FRS000275DA FRS000284BD		Y	N
-21.41	67.18	Harris Crater 3	FRT00008CF6		Y	N
-22.51	66.99	Harris Crater 4	FRT00009E25		Y	maybe
-21.96	66.71	Harris Crater 1	FRT00003A2B FRT00018CDA		Y	Y
			FRT00016FE8 FRT0001BC6C			
-21.67	66.59	Harris Crater 2	HRL00013C12		Y	Y
-27.08	57.76	Niستن Crater	FRT0001BBB5		Y	N
-21.67	57.25		FRT000233B9		Y	N
-24.5	28.28	Murray Crater 3	FRT00007532		N	N
-23.62	27.98	Murray Crater 2	FRS0003D1A2 FRS0003BF05		N	Y
-23.33	27.42	Murray Crater 1	FRT00016438		maybe	N
44.69	8.37	Semeykin	FRT00009E68		maybe	Y
36.7	-0.1	OxusCavus	FRT0000A3D8		maybe	Y
35.92	-8.18	Eden Patera	FRT0000CE47		Y	Y
-52.89	-13.92		FRT00008999		N	maybe
17.7	-23.93	Oxia Planum 1	FRT00009A16		Y	N
17.68	-24.01	Oxia Planum 2	ATU0003D04C ATU00038B10		Y	Y
18.17	-24.18		FRT00004686		Y	N
-23.18	-33.16		FRT0000524A		Y	N
-23.7	-33.6	Eberswalde	FRT00009C06 FRT000060DD	Malin & Edgett (2003), Moore et al. (2003)	Y	Y
-26.69	-34.46	Holden1	FRT0000474A		Y	Y
-26.95	-34.75	Holden2	FRT00009172 FRT00004F2F	Pondrelli et al. (2005), Grant & Parker (2002)	Y	N
			FRT000064B3			
-26.66	-34.78	Holden3	FRT0000C1D1 FRT00006246		Y	N
			HRL00011A15 HRL0000BF84			
-20.48	-35.55	Gringauz Crater	HRL00017EDB		Y	N
11.43	-44.92		FRT0000CCB1		N	N
11.79	-45.19		FRS0003157E		N	N
11.43	-45.3		FRT00004A9A		N	N
11.81	-46.15		FRS0003134F		Y	N

**Table A1**  
(Continued)

LAT	LON	Name	CRISM	Previously Reported	Other Hydrated Minerals	Silica Detections
11.72	-46.76	Magong Crater	FRT00024155 FRT000245E2 HRL0001176F	Hauber et al. (2009)	Y	N
8.5	-48.1		FRT000098B5	Harrison & Grimm (2005)	N	N
8.38	-49.14	Xanthe	HRL0000AB77 HSP00026994		Y	Y
-28.5	-51.3	Ritchey Crater	FRT0000A0B7 FRT00007C34 FRT0000AC1F		Y	Y
2.58	-51.69	Camichel	HRL0000927F HRL0000985E		Y	Y
17.91	-53.78	Maja Valles	HRL0000B48B MSP00004140 FRT000137AE		N	N
33.25	-54.96		FRT000137AE		N	N
-14.97	-60.15	CopratesChasma	FRT00007203 MSP00005107	Di Achille et al. (2006b)	Y	Y
-9.81	-76.47	MeasChasma2	FRT00009B66 FRT000109B6		Y	Y
-9.46	-76.7	MelasChasma1	FRT0000AD3D HRL000134A3 HSP000261DB		Y	maybe
-39.19	-103.02	Claritas Fossae	FRT0000944A FRT0001BA41	Mangold & Ansan (2006)	N	Y
-50.94	-114.35	PorterCrater	HRL00011B83	Kraal et al. (2008a)	N	N
-7.95	-146.56	Amazonis	FRT00014A90 FRT0001BB1F FRT0000BB36 FRT000179D3	Cabrol & Grin (2001)	N	Y
-33.4	-154.5		FRT0000BB36 FRT000179D3		N	N
-40.26	-175.17	Simois Colles	FRT00016E5C		N	N
-23.5	-12.1	Milna	HRS00002FAA	Irwin et al. (2005)	N	N
-5.37	137	Gale	FRT000045F2	Cabrol & Grin (2001)	Y	Y
-15.54	175.56	Gusev	FRT0000595C	Cabrol & Grin (1999)	N	N
-5	-147.21	Senus Vallis	FRT00006264	Di Achille & Hynek (2010)	N	N
22.16	66.94	Baldet	FRT00008D46	Kraal et al. (2008a)	Y	Y
-7.75	148.47		FRT0000A0AC	Di Achille & Hynek (2010)	Y	N
12	-52.7		HRL0000AA4B	Cabrol & Grin (1999)	N	N
11.4	-51.3		FRT0000B0EC	Di Achille & Hynek (2010)	Y	N
27.9	11.6		FRT0000B18B	Irwin et al. (2005)	N	N
-8.6	-159.27		FRT0000BCBD	Ori et al. (2000)	N	N
-15.65	-155.2		FRT0000C165	Ori et al. (2000)	N	N
-9.88	-53.75		HRL0000CD5A	Di Achille & Komatsu (2008)	N	N
4.27	-44.15		HRS0000D035	Di Achille et al. (2007)	Y	N
-1.59	58.19		FRT00011AD5	Kraal et al. (2008a)	N	N
-6.25	-149.47		HRL00011B87	Ori et al. (2000)	Y	N
30.9	12.3		FRT00014A4F	Grant & Schultz (1993)	N	N
-7.98	-3.86		FRT00016CC6	Kraal et al. (2008a)	N	N
28.1	27.2		FRT00016F92	McGill (2002)	Y	N
-27.85	-27.3		FRT00018DEA	Kraal et al. (2008a)	N	N
5.13	-58.6		FRT000199E0	Cabrol & Grin (2001)	Y	N
33.9	17.5	Ismenius Cavus 1	FRT00019B14	Cabrol & Grin (1999)	N	N
-7.7	148.48		HRL0001FDA9	Di Achille & Hynek (2010)	N	N
29.1	84.24		FRT00021F96	Kraal et al. (2008a)	Y	N
34.3	18.1	Ismenius Cavus 2	FRT0002337B	Cabrol & Grin (1999)	N	N
18.25	-37		ATO0002FE3C	Kraal et al. (2008a)	N	N
22.08	73.18		FRS000301CF	Kraal et al. (2008a)	N	N
12	-45		FRS0003157E	Hauber et al. (2009)	Y	N
23.21	15.82		FRS0003284A	Kraal et al. (2008a)	Y	N
-9.68	148.8		FRS00039875	Di Achille & Hynek (2010)	N	N
-50.71	-113.71			Kraal et al. (2008a)		
-39.2	-103.4			Mangold & Ansan (2006)		
-33.28	84.38			Kraal et al. (2008a)		
-27.9	83.1			Moore & Howard (2005)		
-27	-34.45			Pondrelli et al. (2005)		
-26.8	-34.5			Grant & Parker (2002)		
-23.8	-33.7			Malin & Edgett (2003), Moore et al. (2003)		
-19.81	123.29			Kraal et al. (2008a)		
-19.08	-6.35			Irwin et al. (2005)		
-15	-60.3			Di Achille et al. (2006b)		
-10.43	144.6			Di Achille & Hynek (2010)		
-9.2	149.73			Di Achille & Hynek (2010)		
-7.96	-146.58			Cabrol & Grin (2001)		
-6.53	141.14			Di Achille & Hynek (2010)		

**Table A1**  
(Continued)

LAT	LON	Name	CRISM	Previously Reported	Other Hydrated Minerals	Silica Detections
-6.52	141.72			Di Achille & Hynek (2010)		
-5.8	137.3			Cabrol & Grin (2001)		
-5.62	140.3			Di Achille & Hynek (2010)		
-5.15	132.85			Irwin et al. (2004)		
-3.7	142.62			Di Achille & Hynek (2010)		
-3.65	132.7			Irwin et al. (2004)		
2.1	121.6			Irwin et al. (2005)		
2.3	-51.7			Hauber et al. (2009)		
3.1	-43.45			Di Achille et al. (2007)		
6.75	151.1			Williams & Edgett (2005)		
8.5	-49.8			Di Achille et al. (2006a)		
8.5	-48			Harrison & Grimm (2005)		
8.95	-15.76			Di Achille & Hynek (2010)		
9.8	-49.4			Hauber et al. (2009)		
11.9	-46.8			Hauber et al. (2009)		
18.4	77.6			Fassett & Head (2005)		
18.45	77.61			Fassett & Head (2005)		
19.11	-19.71			Kraal et al. (2008a)		
19.42	36.03			Kraal et al. (2008a)		
20.65	-35.72			Kraal et al. (2008a)		
22.11	-39.45			Kraal et al. (2008)		
22.31	36.91			Kraal et al. (2008a)		
23	74.2			Kraal et al. (2008a)		
23.47	27.05			Kraal et al. (2008a)		
23.61	28.02			Kraal et al. (2008a)		
24.65	28.28			Kraal et al. (2008a)		
26.31	-33.91			Kraal et al. (2008a)		
26.85	-28.08			Kraal et al. (2008a)		
27	27.3			Kraal et al. (2008a)		
27.59	83.26			Kraal et al. (2008a)		
28	26.7			McGill (2002)		
29.5	25.7			McGill (2002)		
32.67	7.04			Di Achille & Hynek (2010)		
35.13	-55.54			Di Achille & Hynek (2010)		
35.5	26.3			McGill (2002)		
37.4	8.38			Di Achille & Hynek (2010)		

**Appendix B****Representative Spectra for All Fan and Delta Sites**

For reference, we include the typical spectra acquired for silica-bearing deposits for alluvial fans and deltas in Table 1 (Figure B1), excluding those with an ambiguous context. The

spectral classes are classified based on band-depth thresholds, as shown in Figure B2. Due to the subtle features highlighted by the CRC parameter, more than one spectrum is selected for each location. Here we provide the CRC parameter calculations for all spectra analyzed in this study (Figure B3).



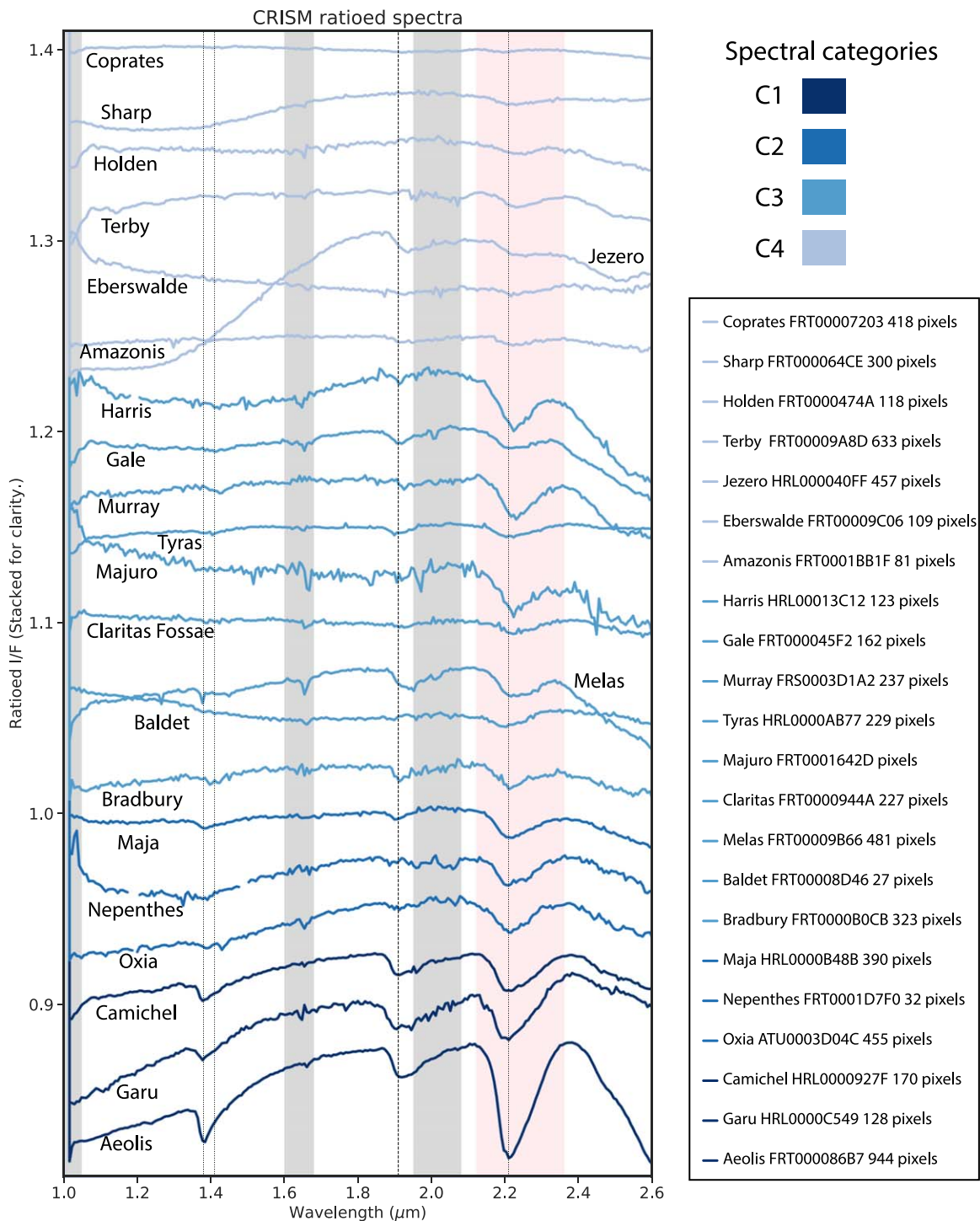


**Figure B1.** Types of silica spectra from all sites with alluvial fan or delta deposits, excluding silica deposits with ambiguous context.

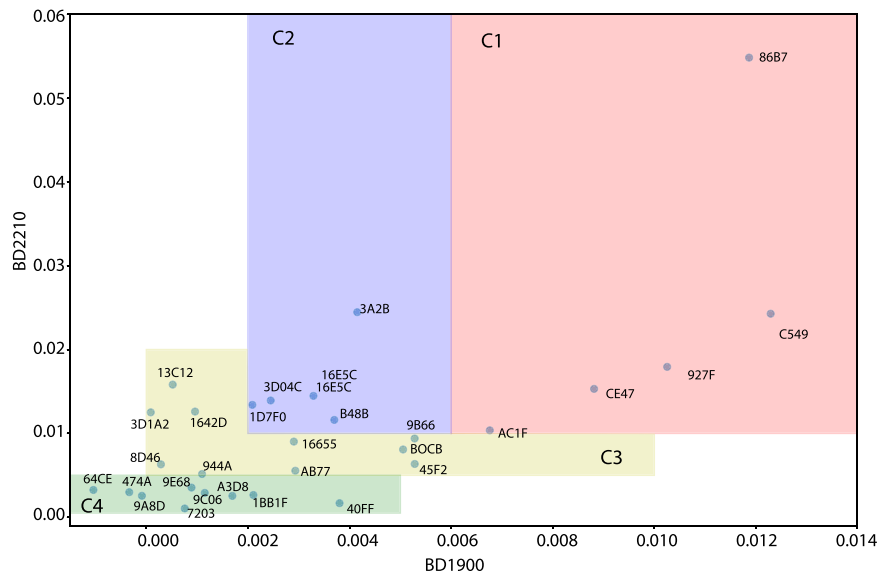


**Figure B2.** Classification of spectral categories based on the classic band-depth formula. The data for the threshold limits and band-depth calculations are provided as data behind the figure.

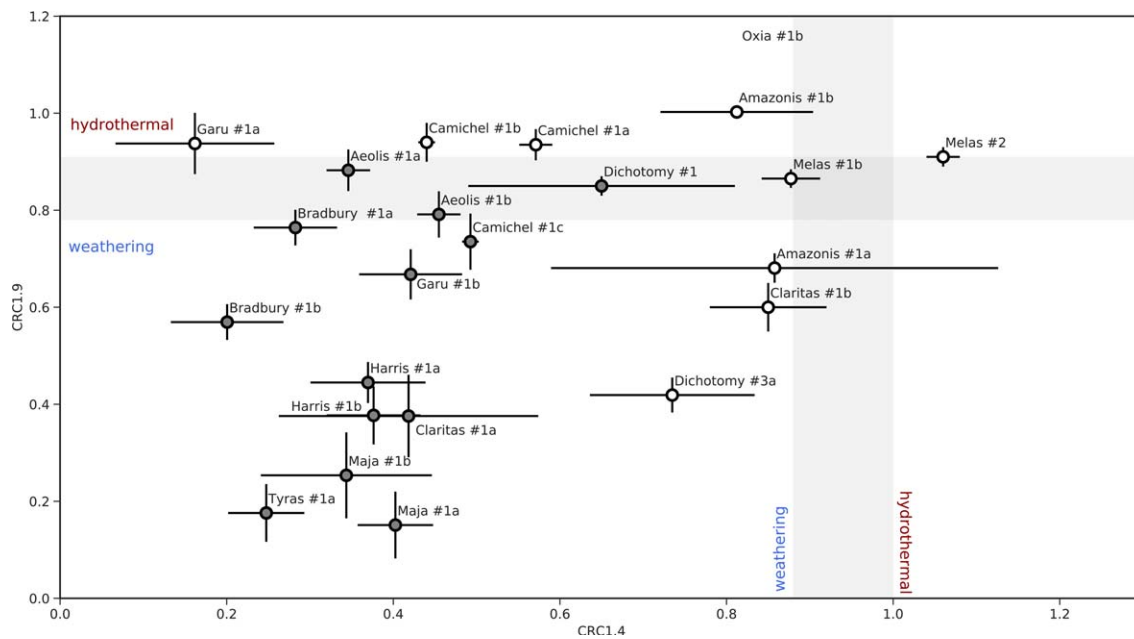


**Figure B3.** The CRC parameters of silica spectra compared to previous lab analyses and other Mars locations (Pineau et al. 2020). Plots of spectral parameters showing differentiating features between silica formation in hydrothermal versus low-temperature weathering systems. Here, the CRC1.9 parameter is highly sensitive to the CO<sub>2</sub> atmospheric residual. The CRC1.4 parameter could be affected by the low signal-to-noise ratio at this wavelength. Data points of lower confidence levels are shown with empty circles. The data and information on the spectra used to make these plots are provided as data behind the figure (see Figure B2).

### Appendix C Hydrated Silica Deposit at Maja Valles

We show the example of the Maja Valles fan deposit. At this location, silica detection is not directly correlated with a

specific fan/delta morphology but is likely the result of past fluvial activities. Other than the main outflow channel (Maja Valles) in which the silica is found, there are two smaller, likely more recent channels (indicated as A and B in Figure C1), which may also have contributed.

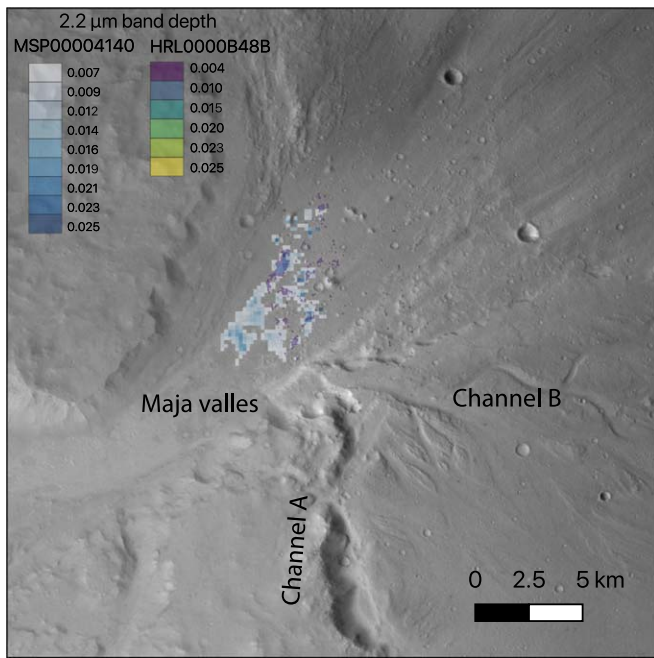


**Figure C1.** Hydrated silica detection at the terminal deposit of Maja Valles. Both the multispectral tile (MSP00004140) and hyperspectral half-resolution tile (HRL0000B48B) are found with this spectral signature. Here, the band depths of these two images are highlighted using different color scales.

#### Appendix D Crater Count for Aeolis Fan

Crater count has been performed on the crater floor unit of the Aeolis fan. Because the fan deposit overlies the crater floor unit, the Aeolis fan likely formed after  $\sim 3.5$  Ga (Figure D1).

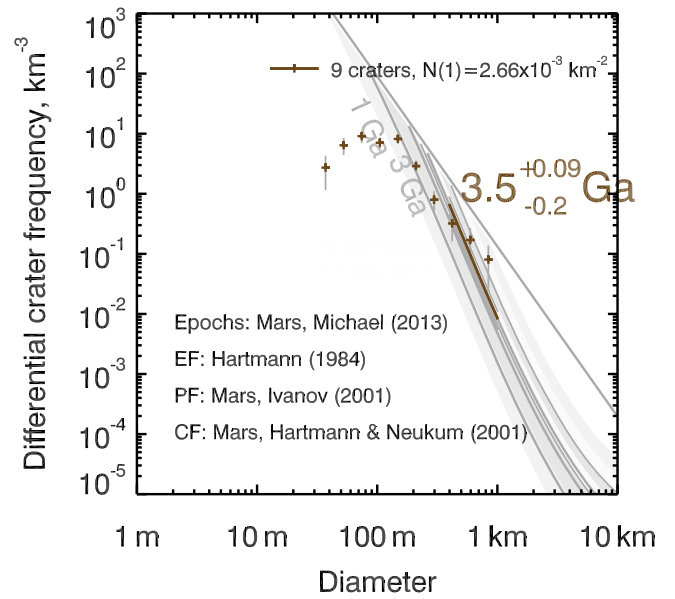


**Figure D1.** Crater count ages of the Aeolis fan crater floor unit.

#### Appendix E Solubility and Temperature of a Silica-bearing Aqueous Solution

Here we show the calculated solubility ranges of silica based on observation compared with the silica solubility curve correlation with temperature and pH (Figure E1), following Equations (6) and (7). The silica dissolved in water remains mostly monomeric silicic acid until  $\text{pH} = 9\text{--}10$ . The silica solubility is calculated based on the equilibrium constant of the first ionic dissociation of silicic acid.

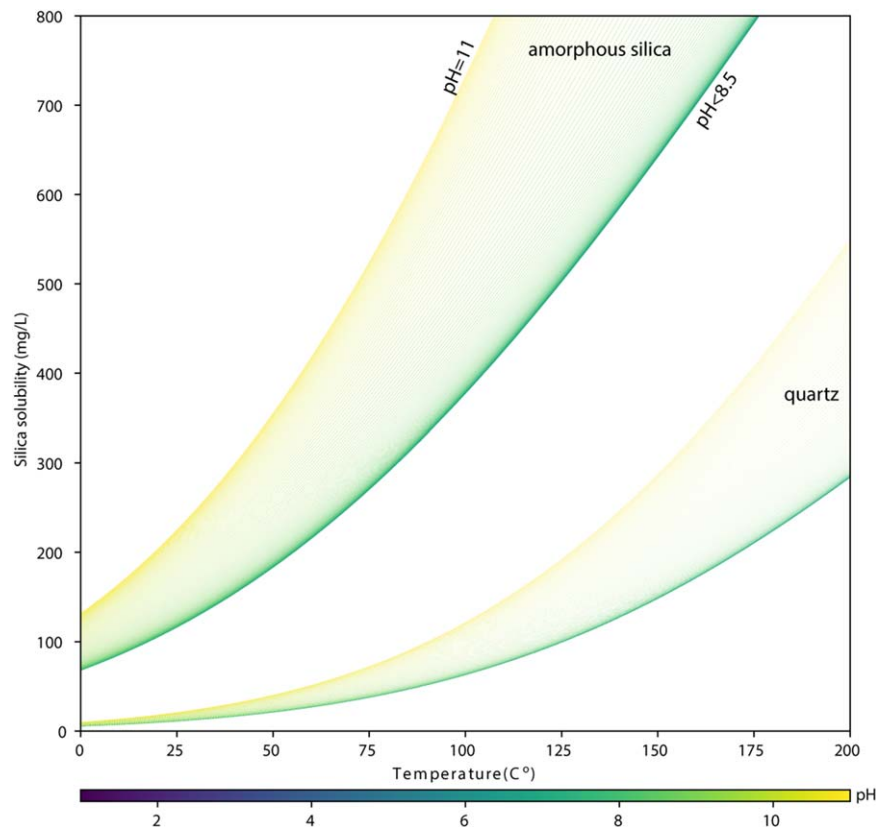


**Figure E1.** Silica solubility ranges calculated for quartz and amorphous silica.

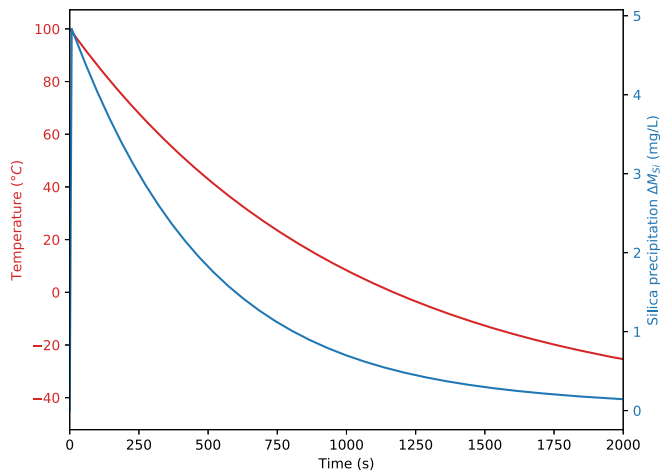


**Figure E2.** Temperature decay and silica precipitation model. The red curve represents the decaying temperature of the liquid solution. The blue curve shows the mass of silica precipitated per second.

We also present the simplistic model of the predicted amount of silica precipitation prediction at neutral pH in an equilibrium water system. We assume an initial temperature  $T_i = 373$  K and Mars typical surface condition  $T_s = 228$  K.  $k$  is the heat transfer coefficient, assumed to be  $0.001 \text{ W m}^{-2} \text{ K}^{-1}$ :

$$T(t) = (T_i - T_s)e^{-kt} + T_s. \quad (\text{E1})$$

The solubility of silica at a given temperature is calculated following Equation (6). As shown in the plot (Figure E2), the amount of silica precipitated per second is expected to decay exponentially as the temperature decays with time.

### Appendix F

#### Volume Measurements of Select Fans and Deltas










Based on topography data from HiRISE and CTX stereo images, detailed volumetric measurements have been made on five typical fans with continuous silica deposits. Table F1 gives the detailed results of the measurements.



**Table F1**  
Volume Measurements for Select Locations

	Unit	Aeolis	Camichel	Garu	Claritas Fossae	Amazonis
HiRISE image		ESP_014159_1670 ESP_020106_1670	ESP_027287_1830 PSP_006941_1825	ESP_015953_1735 ESP_056765_1735 ESP_018366_1735 PSP_009279_1735	PSP_006798_1405 ESP_034014_1405 ESP_034159_1405	PSP_007696_1720 ESP_042666_1720
HiRISE stereo		[014159_1670, 020106_1670]				[007696_1720, 042666_1720]
CTX stereo			[024109_1823, 025388_1823]	[009729_1735, 015953_1735] [009729_1735, 009874_1735]	[006798_1405, 010292_1406]	[007696_1714, 029084_1741]
Fan length	km	2.013	10.9	11.3	7.1	5.76
Fan width	km	1.585	9.46	7.53	8.5	4.4
Fan aspect ratio		1.27	1.15	1.5	0.84	1.31
Fan thickness	km	0.15	0.52	1.1	0.56	0.47
Fan surface area	km <sup>2</sup>	2.33	96.09	53.92	46.4	13.82
Fan gradient		0.0745	0.05	0.09	0.07	0.08
Maximum fan volume	km <sup>3</sup>	0.15	17.99	20.2	17.33	7.07
Apex elevation	m	-520	-1638	-2006	2744	-1132
Fan base elevation	m	-670	-2153	-3115	2180	-1606
Silica outcrop thickness	km	0.15	0.05	0.05	0.01	0.1
Max silica volume	km <sup>3</sup>	0.15	4.8	2.7	0.26	2.07

## ORCID iDs

Lu Pan  <https://orcid.org/0000-0002-8151-2125>  
 John Carter  <https://orcid.org/0000-0002-2698-6926>  
 Cathy Quantin-Nataf  <https://orcid.org/0000-0002-8313-8595>  
 Maxime Pineau  <https://orcid.org/0000-0002-1439-8131>  
 Boris Chauviré  <https://orcid.org/000-0003-0431-6312>  
 Nicolas Mangold  <https://orcid.org/0000-0002-0022-0631>  
 Laetitia Le Deit  <https://orcid.org/0000-0003-1361-5170>  
 Benjamin Rondeau  <https://orcid.org/0000-0003-2954-2770>  
 Vincent Chevrier  <https://orcid.org/0000-0002-1111-587X>

## References

- Abu-Mahfouz, I., Cartwright, J., Idiz, E., Hooker, J. N., & Robinson, S. A. 2020, *Geo*, **48**, 483
- Alexander, G. B., Heston, W. M., & Iler, R. K. 1954, *JPhCh*, **58**, 453
- Anderson, J., & Wickersheim, K. 1964, *SurSc*, **2**, 252
- Ansan, V., Loizeau, D., Mangold, N., et al. 2011, *Icar*, **211**, 273
- Baker, V. R., & Kochel, R. C. 1979, *JGRB*, **84**, 7961
- Bandfield, J. L. 2008, *GeoRL*, **35**, L12205
- Bandfield, J. L., Amador, E. S., & Thomas, N. H. 2013, *Icar*, **226**, 1489
- Beyer, R. A., Alexandrov, O., & McMichael, S. 2018, *E&SS*, **5**, 537
- Bishop, J. L., Dobra, E. Z. N., McKeown, N. K., et al. 2008, *Sci*, **321**, 830
- Bishop, J. L., Tirsch, D., Tornabene, L. L., et al. 2013, *JGRE*, **118**, 487
- Blissenbach, E. 1964, *GSAB*, **65**, 175
- Boboň, M., Christy, A. A., Klivanec, D., & Illášová, L. 2011, *PCM*, **38**, 809
- Bramble, M. S., Goudge, T. A., Milliken, R. E., & Mustard, J. F. 2019, *Icar*, **319**, 363
- Bristow, T. F., & Milliken, R. E. 2011, *CCM*, **59**, 339
- Cabrol, N., & Grin, E. A. 2001, *Icar*, **149**, 291
- Cabrol, N. A., & Grin, E. A. 1999, *Icar*, **142**, 160
- Carter, J., Poulet, F., Bibring, J.-P., Mangold, N., & Murchie, S. 2013a, *JGRE*, **118**, 831
- Carter, J., Poulet, F., Mangold, N., et al. 2012, *LPSC*, **43**, 1978
- Carter, J., Poulet, F., Murchie, S., & Bibring, J. 2013b, *P&SS*, **76**, 53
- Carter, J., Quantin, C., Thollot, P., et al. 2016, *LPSC*, **47**, 2064
- Chapman, M. G., Gudmundsson, M. T., Russell, A. J., & Hare, T. M. 2003, *JGRE*, **108**, 5113
- Chauviré, B., Rondeau, B., & Mangold, N. 2017, *EJMin*, **29**, 409
- Chemtob, S. M., Jolliff, B. L., Rossman, G. R., Eiler, J. M., & Arvidson, R. E. 2010, *JGR*, **115**, E04001
- Christensen, P. R., Wyatt, M. B., Glotch, T. D., et al. 2004, *Sci*, **306**, 1733
- Clark, R. N., King, T. V. V., Klejwa, M., Swayze, G. A., & Vergo, N. 1990, *JGR*, **95**, 12653
- Clark, R. N., Swayze, G. A., Wise, R. A., et al. 2007, USGS Digital Spectral Library splib06a, Data Series 231, <https://doi.org/10.3133/ds231>
- Compton, J. S. 1991, *GSAB*, **103**, 625
- Dehouck, E., Mangold, N., Le Mouélic, S., Ansan, V., & Poulet, F. 2010, *P&SS*, **58**, 941
- de Villiers, G., Kleinmans, M. G., & Postma, G. 2013, *JGRE*, **118**, 651
- Di Achille, G., & Hynek, B. M. 2010, *NatGe*, **3**, 459
- di Achille, G., & Komatsu, G. 2008, *LPSC*, **39**, 1608
- Di Achille, G., Ori, G. G., & Reiss, D. 2007, *JGRE*, **112**, E07007
- Di Achille, G., Marinangeli, L., Ori, G. G., et al. 2006a, *JGR*, **111**, E04003
- Di Achille, G., Ori, G. G., Reiss, D., et al. 2006b, *GeoRL*, **33**, L07204
- Dickson, J. L., Kerber, L. A., Fassett, C. I., & Ehlmann, B. L. 2018, *LPSC*, **49**, 2480
- Dietrich, W. E., Bellugi, D. G., Sklar, L. S., et al. 2003, *GMS*, **135**, 103
- Ding, N., Bray, V. J., McEwen, A. S., et al. 2015, *Icar*, **252**, 255
- Dove, P. M. 1995, in *Chemical Weathering Rates of Silicate Minerals*, ed. A. F. White & S. L. Brantley (Berlin: De Gruyter & Co.)
- Ehlmann, B. L., & Edwards, C. S. 2014, *AREPS*, **42**, 291
- Ehlmann, B. L., Mustard, J. F., Fassett, C. I., et al. 2008, *NatGe*, **1**, 355
- Erkeling, G., Reiss, D., Hiesinger, H., et al. 2012, *Icar*, **219**, 393
- Fassett, C. I., & Head, J. W. 2005, *GeoRL*, **32**, L14201
- Fraeman, A. A., Ehlmann, B. L., Arvidson, R. E., et al. 2016, *JGRE*, **121**, 1713
- Frydenvang, J., Gasda, P. J., Hurowitz, J. A., et al. 2017, *GeoRL*, **44**, 4716
- Golombek, M. P., & Bridges, N. T. 2000, *JGRE*, **105**, 1841
- Goudge, T. A., Mustard, J. F., Head, J. W., & Fassett, C. I. 2012, *JGRE*, **117**, E00J21
- Grant, J. A., & Parker, T. J. 2002, *JGRE*, **107**, 5066
- Grant, J. A., & Schultz, P. H. 1993, *JGR*, **98**, 11025
- Grindrod, P. M., West, M., Warner, N. H., & Gupta, S. 2012, *Icar*, **218**, 178
- Grotzinger, J. P., Gupta, S., Malin, M. C., et al. 2015, *Sci*, **350**, aac7575
- Gunnarsson, I., & Arnórsson, S. 2000, *GeCoA*, **64**, 2295
- Harrison, K. P., & Grimm, R. E. 2005, *JGRE*, **110**, E12S16
- Hauber, E., Gwinner, K., Kleinmans, M., et al. 2009, *P&SS*, **57**, 944
- Hauber, E., Platz, T., Reiss, D., et al. 2013, *JGRE*, **118**, 1529
- Horgan, B. H. N., Anderson, R. B., Dromart, G., Amador, E. S., & Rice, M. S. 2020, *Icar*, **339**, 113526
- Hughes, A. C. G. 2012, Master's thesis, Univ. Tennessee
- Irwin, R. P., Howard, A. D., Craddock, R. A., & Moore, J. M. 2005, *JGR*, **110**, E12S15
- Irwin, R. P., Watters, T. R., Howard, A. D., & Zimbleman, J. R. 2004, *JGRE*, **109**, E09011
- Kite, E. S., Sneed, J., Mayer, D. P., & Wilson, S. A. 2017, *GeoRL*, **44**, 3991
- Kleine, B., Stefánsson, A., Halldórsson, S., Whitehouse, M., & Jónsson, K. 2018, *Geochemical Perspectives Letters*, **5**, doi:10.7185/geochemlet.1811
- Kleinmans, M. G., van de Kastele, H. E., & Hauber, E. 2010, *E&PSL*, **294**, 378
- Knoll, A. H., Whittington, H. B., & Morris, S. C. 1985, *RSPTB*, **311**, 111
- Kraal, E. R., Asphaug, E., Moore, J. M., Howard, A., & Bredt, A. 2008a, *Icar*, **194**, 101
- Kraal, E. R., van Dijk, M., Postma, G., & Kleinmans, M. G. 2008b, *Natur*, **451**, 973
- Langer, K., & Florke, O. W. 1974, *Fortschritte der Mineralogie*, **52**, 17
- Lazzeri, K. E., Bebout, G. E., & Geiger, C. A. 2017, *AmMin*, **102**, 686
- Le Deit, L., Flahaut, J., Quantin, C., et al. 2012, *JGRE*, **117**, E00J05
- Le Deit, L., Hauber, E., Fueten, F., et al. 2013, *JGRE*, **118**, 2439
- Ledevin, M. 2013, PhD thesis, Université de Grenoble
- Malin, M. C., Bell, J. F., Cantor, B. A., et al. 2007, *JGR*, **112**, E05S04
- Malin, M. C., & Edgett, K. S. 2003, *Sci*, **302**, 1931
- Mangold, N. 2004, *Sci*, **305**, 78
- Mangold, N., & Ansan, V. 2006, *Icar*, **180**, 75
- Mangold, N., Carter, J., Poulet, F., et al. 2012a, *P&SS*, **72**, 18
- Mangold, N., Dromart, G., Ansan, V., et al. 2020, *AsBio*, **20**, 994
- Mangold, N., Kite, E. S., Kleinmans, M. G., et al. 2012b, *Icar*, **220**, 530
- Masursky, H., Boyce, J. M., Dial, A. L., Schaber, G. G., & Strobell, M. E. 1977, *JGR*, **82**, 4016
- McEwen, A. S., Eliason, E. M., Bergstrom, J. W., et al. 2007, *JGR*, **112**, E05S02
- McGill, G. E. 2002, USGS, I-2746, <https://pubs.usgs.gov/imap/i2746/>
- McLennan, S. M. 2003, *Geo*, **31**, 315
- McLennan, S. M., Bell, J. F., Calvin, W. M., et al. 2005, *E&PSL*, **240**, 95
- McMahon, S., Bosak, T., Grotzinger, J. P., et al. 2018, *JGRE*, **123**, 1012
- Metz, J. M., Grotzinger, J. P., Mohrig, D., et al. 2009, *JGRE*, **114**, E10002
- Milliken, R., Swayze, G., Arvidson, R., et al. 2008, *Geo*, **36**, 847
- Milliken, R. E., & Bish, D. L. 2010, *PMag*, **90**, 2293
- Minitti, M. E., Weitz, C. M., Lane, M. D., & Bishop, J. L. 2007, *JGRE*, **112**, E05015
- Moore, J. M., & Howard, A. D. 2005, *JGRE*, **110**, E04005
- Moore, J. M., Howard, A. D., Dietrich, W. E., & Schenk, P. M. 2003, *GeoRL*, **30**, 2292
- Murchie, S., Arvidson, R., Bedini, P., et al. 2007, *JGRE*, **112**, E05S03
- Murchie, S. L., Seelos, F. P., Hash, C. D., et al. 2009, *JGRE*, **114**, E00D06
- Nickel, E. 1985, *SedG*, **42**, 83
- Opfergelt, S., Georg, R., Burton, K., et al. 2011, *ApGC*, **26**, S115
- Ori, G. G., Marinangeli, L., & Baliva, A. 2000, *JGR*, **105**, 17629
- Palucis, M. C., Dietrich, W. E., Hayes, A. G., et al. 2014, *JGRE*, **119**, 705
- Palucis, M. C., Dietrich, W. E., Williams, R. M. E., et al. 2016, *JGRE*, **121**, 472
- Palucis, M. C., Jasper, J., Garczynski, B., & Dietrich, W. E. 2020, *Icar*, **341**, 113623
- Pan, L., & Ehlmann, B. L. 2014, *GeoRL*, **41**, 1890
- Pan, L., Ehlmann, B. L., Carter, J., & Ernst, C. M. 2017, *JGRE*, **122**, 1824
- Pepin, E., Carretier, S., & Herail, G. 2010, *Geomio*, **122**, 78
- Pineau, M., Le Deit, L., Chauviré, B., et al. 2020, *Icar*, **347**, 113706
- Ping, C. L., Shoji, S., & Ito, T. 1988, *SSAJ*, **52**, 455
- Poitras, J., Cloutis, E., Salvatore, M., et al. 2018, *Icar*, **306**, 50
- Pondrelli, M., Baliva, A., Di Lorenzo, S., Marinangeli, L., & Rossi, A. P. 2005, *JGRE*, **110**, E04016
- Popa, C., Esposito, F., & Colangeli, L. 2010, *LPSC*, **41**, 1807
- Poulet, F., Carter, J., Bishop, J. L., Loizeau, D., & Murchie, S. M. 2014, *Icar*, **231**, 65
- Quantin, C., Allemand, P., Mangold, N., Dromart, G., & Delacourt, C. 2005, *JGRE*, **110**, E12S19
- Quantin-Nataf, C., Carter, J., Mandon, L., et al. 2021, *AsBio*, **21**, 345
- Quantin-Nataf, C., Lozac'h, L., Thollot, P., et al. 2018, *P&SS*, **150**, 157

- Rapin, W., Chauviré, B., Gabriel, T. S. J., et al. 2018, *JGRE*, **123**, 1955
- Rice, M., Bell, J., Cloutis, E., et al. 2010, *Icar*, **205**, 375
- Rice, M., Cloutis, E., Bell, J., et al. 2013, *Icar*, **223**, 499
- Ruesch, O., Hiesinger, H., Cloutis, E., et al. 2015, *Icar*, **258**, 384
- Savitzky, A., & Golay, M. J. E. 1964, *AnaCh*, **36**, 1627
- Seelos, K. D., Seelos, F. P., Viviano-Beck, C. E., et al. 2014, *GeoRL*, **41**, 4880
- Shepard, M. K., & Cloutis, E. 2011, *LPSC*, **42**, 1043
- Shoji, S., & Masui, J.-I. 1971, *Journal of Soil Science*, **22**, 101
- Siever, R. 1962, *JG*, **70**, 127
- Sjöberg, S. 1996, *JNCS*, **196**, 51
- Skok, J. R., Mustard, J. F., Ehlmann, B. L., Milliken, R. E., & Murchie, S. L. 2010, *NatGe*, **3**, 838
- Smith, M. R., Bandfield, J. L., Cloutis, E. A., & Rice, M. S. 2013, *Icar*, **223**, 633
- Squyres, S. W., Arvidson, R. E., Ruff, S., et al. 2008, *Sci*, **320**, 1063
- Steinier, J., Termonia, Y., & Deltour, J. 1972, *AnaCh*, **44**, 1906
- Sun, V. Z., & Milliken, R. E. 2014, *JGRE*, **119**, 810
- Sun, V. Z., & Milliken, R. E. 2015, *JGRE*, **120**, 2293
- Sun, V. Z., & Milliken, R. E. 2018, *GeoRL*, **45**, 10,221
- Tarnas, J. D., Mustard, J. F., Lin, H., et al. 2019, *GeoRL*, **46**, 12,771
- Teece, B. L., George, S. C., Djokic, T., et al. 2020, *AsBio*, **20**, 537
- Thomson, B. J., Bridges, N. T., Milliken, R., et al. 2011, *Icar*, **214**, 413
- Tirsch, D., Bishop, J. L., Voigt, J. R. C., et al. 2018, *Icar*, **314**, 12
- Tosca, N. J., & Knoll, A. H. 2009, *E&PSL*, **286**, 379
- Trewin, N. H. 1996, in *Ciba Foundation Symp.* 131 (New York: Wiley)
- Trower, E. J., & Lowe, D. R. 2016, *PreR*, **281**, 473
- van den Boorn, S. H. J. M., Bergen, M. J. v., Nijman, W., & Vroon, P. Z. 2007, *Geo*, **35**, 939
- Watkins, J. A., Ehlmann, B. L., & Yin, A. 2015, *Geo*, **43**, 107
- Weitz, C., Irwin, R., III, Chuang, F., Bourke, M., & Crown, D. 2006, *Icar*, **184**, 436
- Weitz, C. M., Noe Dobrea, E., & Wray, J. J. 2015, *Icar*, **251**, 291
- Weitz, C. M., Parker, T. J., Bulmer, M. H., Anderson, F. S., & Grant, J. A. 2003, *JGRE*, **108**, 8082
- Williams, L. A., & Crerar, D. A. 1985, *Journal of Sedimentary Petrology*, **55**, 312
- Williams, L. A., Parks, G. A., & Crerar, D. A. 1985, *Journal of Sedimentary Petrology*, **55**, 301
- Williams, R. M., Deanne Rogers, A., Chojnacki, M., et al. 2011, *Icar*, **211**, 222
- Williams, R. M., & Weitz, C. M. 2014, *Icar*, **242**, 19
- Williams, R. M. E., & Edgett, K. S. 2005, *LPSC*, **36**, 1099
- Wilson, S. A., Howard, A. D., Moore, J. M., & Grant, J. A. 2007, *JGRE*, **112**, E08009